K to $\pi\pi$ decay amplitudes from lattice QCD

T. Blum,[1] P. A. Boyle,[2] N. H. Christ,[3] N. Garron,[2] E. Goode,[4] T. Izubuchi,[5,6] C. Lehner,[6]
Q. Liu,[3] R. D. Mawhinney,[3] C. T. Sachrajda,[4] A. Soni,[5] C. Sturm,[7] H. Yin,[3] and R. Zhou[1,8]

(RBC and UKQCD Collaborations)

[1]*Physics Department, University of Connecticut, Storrs, Connecticut 06269-3046, USA*
[2]*SUPA, School of Physics, The University of Edinburgh, Edinburgh EH9 3JZ, UK*
[3]*Physics Department, Columbia University, New York, New York 10027, USA*
[4]*School of Physics and Astronomy, University of Southampton, Southampton SO17 1BJ, UK*
[5]*Brookhaven National Laboratory, Upton, New York 11973, USA*
[6]*RIKEN-BNL Research Center, Brookhaven National Laboratory, Upton, New York 11973, USA*
[7]*Max-Planck-Institut für Physik, Föhringer Ring 6, 80805 München, Germany*
[8]*Department of Physics, Indiana University, Bloomington, Indiana 47405, USA*

We report a direct lattice calculation of the K to $\pi\pi$ decay matrix elements for both the $\Delta I = 1/2$ and $3/2$ amplitudes A_0 and A_2 on $2 + 1$ flavor, domain wall fermion, $16^3 \times 32 \times 16$ lattices. This is a complete calculation in which all contractions for the required ten, four-quark operators are evaluated, including the disconnected graphs in which no quark line connects the initial kaon and final two-pion states. These lattice operators are nonperturbatively renormalized using the Rome-Southampton method and the quadratic divergences are studied and removed. This is an important but notoriously difficult calculation, requiring high statistics on a large volume. In this paper, we take a major step toward the computation of the physical $K \to \pi\pi$ amplitudes by performing a complete calculation at unphysical kinematics with pions of mass 422 MeV at rest in the kaon rest frame. With this simplification, we are able to resolve Re(A_0) from zero for the first time, with a 25% statistical error and can develop and evaluate methods for computing the complete, complex amplitude A_0, a calculation central to understanding the $\Delta = 1/2$ rule and testing the standard model of CP violation in the kaon system.

I. INTRODUCTION

The Cabibbo-Kobayashi-Maskawa (CKM) theory for the weak interactions of the quarks when combined with QCD provides a framework describing in complete detail all the properties and interactions of the six quarks. This framework incorporates the most general assignment of masses and couplings and appears able to explain all observed phenomena in which these quarks participate. However, to date, the nonperturbative character of low-energy QCD has obscured many of the consequences of the CKM theory. In particular, both the direct CP violation seen in K meson decay and the factor of 22.5 enhancement of the $I = 0$, $K \to \pi\pi$ decay amplitude A_0 relative to the $I = 2$ amplitude A_2 (the $\Delta I = 1/2$ rule) lack a quantitative explanation.

Wilson coefficients evaluated at a QCD scale of about 2 GeV represent the short-distance physics and can be evaluated from the CKM theory using QCD and electroweak perturbation theory. However, these factors explain only a factor of 2 enhancement of the $I = 0$ amplitude [1,2]. The remaining enhancement must arise from the hadronic matrix elements which require nonperturbative treatment.

Direct CP violation in kaon decays provides a critical test of the standard model's CKM mechanism of CP violation. While 40 years of experimental effort have produced the measured result Re(ϵ'/ϵ) = 1.65(26) × 10^{-3} [3], with only a 16% error, there is no reliable theoretical calculation of this quantity based on the standard model. A previous lattice QCD calculation using $2 + 1$ dynamical domain wall fermions failed to give a conclusive result because of the large systematic errors associated with the use of chiral perturbation theory at the scale of the kaon mass [4]. (However, there are ongoing efforts using chiral perturbation theory [5]). Earlier quenched results [6,7] are subject to this same difficulty together with uncontrolled uncertainties associated with quenching [8–10].

A direct lattice calculation of $K \to \pi\pi$ decay is extremely important to provide an explanation for the $\Delta I = 1/2$ rule and to test the standard model of CP violation from first principles. This is an unusually difficult calculation because of the presence of disconnected graphs. However, with the continuing increase of available computing power and the development of improved algorithms, calculations with disconnected graphs are now no longer out of reach. In fact, our recent successful calculation of the masses and mixing of the η' and η mesons [11] was

carried out in part to develop and test the methods needed for the calculation presented here. In this paper, we present a first direct calculation of the complete $K^0 \to \pi\pi$ decay amplitude. At this stage, we work with the simplified kinematics of a threshold decay in which the kaon is at rest and decays into two pions each with zero momentum and with mass one-half that of the kaon. The calculation with this choice of kinematics still contains the main difficulties we need to overcome in order to be able to compute the physical $K \to \pi\pi$ decay amplitudes; i.e. the presence of disconnected diagrams coupled with the need to subtract ultraviolet power divergences. However, as explained below, with the pions at rest we are able to generate sufficient statistics to explore how to handle these difficulties. We stress that at this simplified choice of kinematics, we compute the $K \to \pi\pi$ amplitudes directly and completely.

In order to calculate the decay amplitudes, we perform a direct, brute force calculation of the required weak matrix elements. The isospin zero $\pi - \pi$ final state implies the presence of disconnected graphs in correlation functions and makes the calculation very difficult. For these graphs, the noise does not decrease with increasing time separation between the source and sink, while the signal does. Therefore, substantial statistics are needed to get a clear signal. This difficulty is compounded by the presence of diagrams which diverge as $1/a^2$ as the continuum limit is approached (a is the lattice spacing). While these divergent amplitudes must vanish for a physical, on-shell decay they substantially degrade the signal to noise ratio even for an energy-conserving calculation such as this one. Studying the properties of the $1/a^2$ terms and learning how to successfully subtract them is one of the important objectives of this calculation. The chiral symmetry needed to control operator mixing is provided by our use of domain wall fermions.

Recognizing the difficulty of this problem, we choose to perform this first calculation on a lattice which is relatively small compared to those used in other recent work and to use a somewhat heavy pion mass ($m_\pi \approx 421$ MeV) so we can more easily collect large statistics. We concentrate on exploring and reducing the statistical uncertainty since the primary goal of this work is to extract a clear signal for these amplitudes. Therefore, the quoted errors on our results are statistical only.

The main objective of this paper is to calculate the $\Delta I = 1/2$ decay amplitude A_0. A calculation of the $\Delta I = 3/2$ part is included here for comparison and completeness. A much more physical calculation of this $\Delta I = 3/2$ amplitude alone can be found in [12]. In the case of the $I = 2$ final state, no disconnected diagrams appear, there are no divergent eye diagrams and isospin conservation requires that four valence quark propagators must join the kaon and weak operator with the operators creating the two final-state pions. This allows physical kinematics with nonzero

final momenta to be achieved by imposing antiperiodic boundary conditions on one species of valence quark [13,14]. As a result, the preliminary calculation of A_2 reported in Ref. [12] is performed at almost physical kinematics on a lattice of spatial size 4.5 fm and determines complex A_2 with controlled errors of $O(10\%)$. The present work is intended as the first step toward an equally physical but much more challenging calculation of A_0.

While we do not employ physical kinematics, the final results for the complex amplitudes A_0 and A_2 presented in this paper are otherwise physical. In particular, we use Rome-Southampton methods [15] to change the normalization of our bare lattice four-quark operators to that of the RI/MOM scheme. A second conversion to the $\overline{\text{MS}}$ scheme is then performed using the recent results of Ref. [16]. Finally these $\overline{\text{MS}}$-normalized matrix elements are combined with the appropriate Wilson coefficients [17], determined in this same scheme, to obtain our results for A_0 and A_2. Because of our unphysical, threshold kinematics and focus on controlling the statistical errors associated with the disconnected diagrams, we do not estimate the size of possible systematic errors. Similarly, we do not include the systematic or statistical errors associated with the Rome-Southampton renormalization factors, both of which could be made substantially smaller than our statistical errors when required.

This paper is organized as follows. We first summarize our computational setup, including our strategy to collect large statistics. Next, we discuss our results for $\pi - \pi$ scattering which are a by-product of the necessary characterization of the operator creating the $\pi - \pi$ final state and are also needed to evaluate the Lellouch-Lüscher, finite-volume correction [18]. After a section giving the details of the $K^0 \to \pi\pi$ contractions, we provide our numerical results for the $K^0 \to \pi\pi$ decay amplitudes for both the $\Delta I = 3/2$ and $1/2$ channels. The details of the operator renormalization required by the Wilson coefficients which we use are presented in Appendix A. Finally, we present our conclusions and discuss future prospects.

II. COMPUTATIONAL DETAILS

Our calculation uses the Iwasaki gauge action with $\beta = 2.13$ and $2 + 1$ flavors of domain wall fermions (DWF). While the computational costs of DWF are much greater than those of Wilson or staggered fermions, as has been shown in earlier papers [6,7,19,20], accurate chiral symmetry at short distances is critical to avoid extensive operator mixing, which would make the lattice treatment of $\Delta S = 1$ processes much more difficult.

We use a single lattice ensemble with space-time volume $16^3 \times 32$, a fifth-dimensional extent of $L_s = 16$ and light and strange quark masses of $m_l = 0.01$, $m_s = 0.032$, respectively. This ensemble is similar to the $m_l = 0.01$ ensemble reported in Ref. [21] except we use the improved RHMC-II algorithm of Ref. [22] and a more physical value

for the strange quark mass. The inverse lattice spacing for these input parameters was determined to be 1.73(3) GeV and the residual mass is $m_{\mathrm{res}} = 0.00308(4)$ [22]. The total number of configurations we used is 800, each separated by 10 time units. We initially generated an ensemble one-half of this size. When our analysis showed a nonzero result for $\mathrm{Re}A_0$, we then doubled the size of the ensemble to assure ourselves that the result was trustworthy and to reduce the resulting error. We have performed the analysis described below both by treating the results from each configuration as independent and by grouping them into blocks. The resulting statistical errors are independent of block size suggesting that the individual configurations are essentially uncorrelated for our observables.

We use antiperiodic boundary conditions in the time direction, and periodic boundary conditions in the space directions for the Dirac operator. The propagators (inverses of the Dirac operator) are calculated using a Coulomb gauge-fixed wall source (used for meson propagators) and a random wall source (used to calculate the loops in the $type3$ and $type4$ graphs shown in Figs. 5 and 6 below) for each of the 32 time slices in our lattice volume. The details of our choice of sources are provided in Appendix B. For each time slice and source type, twelve inversions are required corresponding to the possible 3 color and 4 spin choices for the source. Thus, all together we carry out 768 inversions for each quark mass on a given configuration. As will be shown below, this large number of inversions, performed on 800 configurations, provides the substantial statistics needed to resolve the real part of the $I = 0$ amplitude A_0 with 25% accuracy.

The situation described above in which 768 Dirac propagators must be computed on a single gauge background is an excellent candidate for the use of deflation techniques. The overhead associated with determining a set of low eigenmodes of this single Dirac operator can be effectively amortized over the many inversions in which those low modes can be used. Our $m_l = 0.01$, light quark inversions are accelerated by a factor of 2–3 by using exact, low-mode deflation [23] in which we compute the Dirac eigenvectors with the smallest 35 eigenvalues and limit the conjugate gradient inversion to the remaining orthogonal subspace.

In order to obtain energy-conserving $K^0 \to \pi\pi$ decay amplitudes, the mass of the valence strange quark in the kaon is assigned a value different from that appearing in the fermion determinant used to generate the ensembles,

i.e. the strange quark is partially quenched. Since the mass of the dynamical strange quark is expected to have a small effect on amplitudes of the sort considered here [22,24], this use of partial quenching is appropriate for the purposes of this paper. Valence strange quark masses are chosen to be $m_s = 0.066$, 0.099 and 0.165, which are labeled 0, 1, and 2, respectively. The resulting kaon masses are shown in Table I. In the following section, we will see that by using these values for m_s we can interpolate to energy-conserving decay kinematics for both the $I = 2$ and $I = 0$ channels.

III. TWO-PION SCATTERING

The $\pi - \pi$ scattering calculation requires 4 contractions which we have labeled direct (D), cross (C), rectangle (R), and vacuum (V) as in Ref. [25] and which are shown in Fig. 1. For convenience, the minus sign arising from the number of fermion loops is not included in the definition of these contractions. The vacuum contraction should be accompanied by a vacuum subtraction. These contractions can be calculated in terms of the light quark propagator $L(t_{\mathrm{snk}}, t_{\mathrm{src}})$ for a Coulomb gauge-fixed wall source located at the time t_{src} and a similar wall sink located at t_{snk}. The resulting complete vacuum amplitude, including the vacuum subtraction, is given by

$$
\begin{aligned}
V(t) = \frac{1}{32} \sum_{t'=0}^{31} & \{\langle \mathrm{tr}[L(t', t')L(t', t')^{\dagger}]\mathrm{tr}[L(t + t', t + t') \\
& \times L(t + t', t + t')^{\dagger}]\rangle - \langle \mathrm{tr}[L(t', t')L(t', t')^{\dagger}]\rangle \\
& \times \langle \mathrm{tr}[L(t + t', t + t')L(t + t', t + t')^{\dagger}]\rangle\},
\end{aligned}
\tag{1}
$$

where the indicated traces are taken over spin and color, the hermiticity properties of the domain wall propagator have been used to eliminate factors of γ^5 and we are explicitly combining the results from each of the 32 time slices.

Our results for each of these four types of contractions are shown in the left panel of Fig. 2. Notice that the disconnected (vacuum) graph has an almost constant error with increasing time separation between the source and sink, so it appears to have an increasing error bar in the log plot, while the signal decreases exponentially.

These four types of correlators can be combined to construct physical correlation functions for two-pion states with definite isospin:

TABLE I. Masses of pion and kaons and energies of the two-pion states. Here the subscript $I = 0$ or 2 on the $\pi - \pi$ energy, $E_I^{\pi\pi}$, labels the isospin of the state and $E_0^{\pi\pi\prime}$ represents the isospin zero, two-pion energy obtained when the disconnected graph V is ignored. The superscript (0), (1) or (2) on the kaon mass distinguishes our three choices of valence strange quark mass, $m_s = 0.066$, 0.099 and 0.165, respectively.

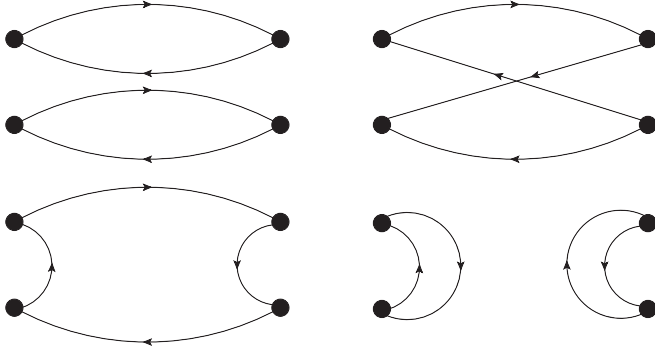| m_π	$E_0^{\pi\pi}$	$E_0^{\pi\pi\prime}$	$E_2^{\pi\pi}$	$m_K^{(0)}$	$m_K^{(1)}$	$m_K^{(2)}$
0.24373(47)	0.443(13)	0.4393(41)	0.5066(11)	0.42599(42)	0.50729(44)	0.64540(49)

FIG. 1.   The four diagrams which contribute to $\pi - \pi$ scattering: direct (D), cross (C), rectangle (R), and vacuum (V), arranged from the left top to right bottom.

$$\langle O_2^{\pi\pi}(t + t')^\dagger O_2^{\pi\pi}(t')\rangle = 2(D(t) - C(t)) \qquad (2)$$

$$\langle O_0^{\pi\pi}(t + t')^\dagger O_0^{\pi\pi}(t')\rangle = 2D(t) + C(t) - 6R(t) + 3V(t). \qquad (3)$$

Here, the operator $O_I^{\pi\pi}(t)$ creates a two-pion state with total isospin I and z-component of isospin $I_z = 0$ using two quark and two antiquark wall-sources located at the time-slice t. As in Eq. (1), we will average over all 32 possible values of common time displacement t' to improve statistics.

The two-pion correlation functions for isospin I and $I_z = 0$ are fit with a functional form $\text{Corr}I(t) = N_I^2\{\exp(-E_I^{\pi\pi}t) + \exp(-E_I^{\pi\pi}(T - t)) + C_I\}$, where the constant C_I comes from the case in which the two pions propagate in opposite time directions. The fitted energies are summarized in Table I. In order to see clearly the effect of the disconnected graph, we also perform the calculation for the $I = 0$ channel without the disconnected graphs. This result is given in Table I with a label with an additional prime ($'$) symbol. The resulting effective mass plots for each case are shown in the right panel of Fig. 2. For comparison, a plot of twice the pion effective mass

is also shown. This figure clearly demonstrates that the two-pion interaction is attractive in the $I = 0$ channel with the finite volume, $I = 0$ $\pi - \pi$ energy $E_0^{\pi\pi}$ lower than $2m_\pi$. In contrast, the $I = 2$ channel is repulsive with $E_2^{\pi\pi}$ larger than $2m_\pi$. The fitted parameters $N_I^{\pi\pi}$ and $E_I^{\pi\pi}$ will be used to extract weak matrix elements from the $K^0 \to \pi\pi$ correlation functions discussed below in which these same operators $O_I^{\pi\pi}(t)$ are used to construct the two-pion states.

IV. CONTRACTIONS FOR $K^0 \to \pi\pi$ DECAYS

The effective weak Hamiltonian describing $K^0 \to \pi\pi$ decay including the u, d, and s flavors as dynamical variables is

$$H_w = \frac{G_F}{\sqrt{2}} V_{ud}^* V_{us} \sum_{i=1}^{10}[(z_i(\mu) + \tau y_i(\mu))]Q_i. \qquad (4)$$

Throughout this paper, we follow the conventions and notation of Ref. [6]. In Eq. (4), the Q_i are the 10 conventional four-quark operators, z_i and y_i are the Wilson coefficients, and τ represents a combination of CKM matrix elements: $\tau = -V_{ts}^* V_{td}/V_{ud}V_{us}^*$. To calculate the decay amplitudes A_2 and A_0, we need to calculate the matrix elements $\langle\pi\pi|Q_i|K^0\rangle$ on the lattice.

We list all of the possible contractions contributing to the matrix elements $\langle\pi\pi|Q_i|K^0\rangle$ in 3–6. There are 48 different contractions which are labeled by circled numbers ranging from 1 to 48, and grouped into four categories labeled as $type1$, $type2$, $type3$, and $type4$ according to their topology. Once we have calculated all of these contractions, the correlation functions $\langle O_I^{\pi\pi}(t_\pi)Q_i(t_{op})K^0(t_K)\rangle$ are then obtained as combinations of these contractions. In order to simplify the following formulae, we use the amplitude $A_{I,i}(t_\pi, t, t_K)$ to represent three point function $\langle O_I^{\pi\pi}(t_\pi)Q_i(t_{op})K(t_K)\rangle$. Using this notation, the $I = 2$ amplitudes can be written
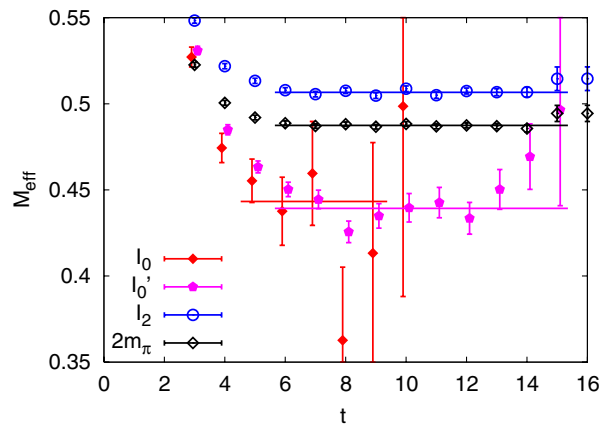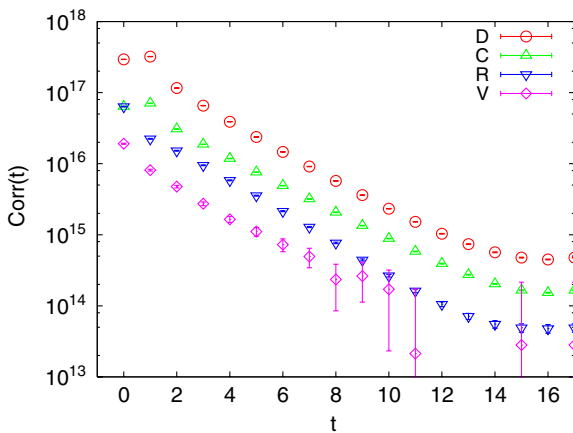

FIG. 2 (color online).   Left: Results for the four types of contractions, direct (D), cross (C), rectangle (R), and vacuum (V) represented by the graphs in Fig. 1. Right: Effective mass plots for correlation functions for states with isospin two (I_2), isospin zero (I_0), isospin zero without the disconnected graph (I_0') and twice the pion effective mass ($2m_\pi$).

$$A_{2,1}(t_\pi, t_{\mathrm{op}}, t_K) = i\sqrt{\frac{2}{3}}\{① - ⑤\} \tag{5a}$$

$$A_{2,2}(t_\pi, t_{\mathrm{op}}, t_K) = i\sqrt{\frac{2}{3}}\{② - ⑥\} \tag{5b}$$

$$A_{2,3}(t_\pi, t_{\mathrm{op}}, t_K) = 0 \tag{5c}$$

$$A_{2,4}(t_\pi, t_{\mathrm{op}}, t_K) = 0 \tag{5d}$$

$$A_{2,5}(t_\pi, t_{\mathrm{op}}, t_K) = 0 \tag{5e}$$

$$A_{2,6}(t_\pi, t_{\mathrm{op}}, t_K) = 0 \tag{5f}$$

$$A_{2,7}(t_\pi, t_{\mathrm{op}}, t_K) = i\sqrt{\frac{3}{2}}\{③ - ⑦\} \tag{5g}$$

$$A_{2,8}(t_\pi, t_{\mathrm{op}}, t_K) = i\sqrt{\frac{3}{2}}\{④ - ⑧\} \tag{5h}$$

$$A_{2,9}(t_\pi, t_{\mathrm{op}}, t_K) = i\sqrt{\frac{3}{2}}\{① - ⑤\} \tag{5i}$$

$$A_{2,10}(t_\pi, t_{\mathrm{op}}, t_K) = i\sqrt{\frac{3}{2}}\{② - ⑥\} \tag{5j}$$

and in the $I = 0$ case,

$$A_{0,1}(t_\pi, t_{\mathrm{op}}, t_K) = i\frac{1}{\sqrt{3}}\{-① - 2\cdot⑤ + 3\cdot⑨ + 3\cdot⑰ - 3\cdot㉝\} \tag{6a}$$

$$A_{0,2}(t_\pi, t_{\mathrm{op}}, t_K) = i\frac{1}{\sqrt{3}}\{-② - 2\cdot⑥ + 3\cdot⑩ + 3\cdot⑱ - 3\cdot㉞\} \tag{6b}$$

$$A_{0,3}(t_\pi, t_{\mathrm{op}}, t_K) = i\sqrt{3}\{-⑤ + 2\cdot⑨ - ⑬ + 2\cdot⑰ + ㉑ - ㉕ - ㉙ - 2\cdot㉝ - ㊲ + ㊶ + ㊺\} \tag{6c}$$

$$A_{0,4}(t_\pi, t_{\mathrm{op}}, t_K) = i\sqrt{3}\{-⑥ + 2\cdot⑩ - ⑭ + 2\cdot⑱ + ㉒ - ㉖ - ㉚ - 2\cdot㉞ - ㊳ + ㊷ + ㊻\} \tag{6d}$$

$$A_{0,5}(t_\pi, t_{\mathrm{op}}, t_K) = i\sqrt{3}\{-⑦ + 2\cdot⑪ - ⑮ + 2\cdot⑲ + ㉓ - ㉗ - ㉛ - 2\cdot㉟ - ㊴ + ㊸ + ㊼\} \tag{6e}$$

$$A_{0,6}(t_\pi, t_{\mathrm{op}}, t_K) = i\sqrt{3}\{-⑧ + 2\cdot⑫ - ⑯ + 2\cdot⑳ + ㉔ - ㉘ - ㉜ - 2\cdot㉜ - ㊵ + ㊹ + ㊽\} \tag{6f}$$

$$A_{0,7}(t_\pi, t_{\mathrm{op}}, t_K) = i\frac{\sqrt{3}}{2}\{-③ - ⑦ + ⑪ + ⑮ + ⑲ - ㉓ + ㉗ + ㉛ - ㉟ + ㊴ - ㊸ - ㊼\} \tag{6g}$$

$$A_{0,8}(t_\pi, t_{\mathrm{op}}, t_K) = i\frac{\sqrt{3}}{2}\{-④ - ⑧ + ⑫ + ⑯ + ⑳ - ㉔ + ㉘ + ㊳ - ㉜ + ㊵ - ㊹ - ㊽\} \tag{6h}$$

$$A_{0,9}(t_\pi, t_{\mathrm{op}}, t_K) = i\frac{\sqrt{3}}{2}\{-① - ⑤ + ⑨ + ⑬ + - ㉑ + ㉕ + ㉙ - ㉝ + ㊲ - ㊶ - ㊺\} \tag{6i}$$

$$A_{0,10}(t_\pi, t_{\mathrm{op}}, t_K) = i\frac{\sqrt{3}}{2}\{-② - ⑥ + ⑩ + ⑭ + ⑱ - ㉒ + ㉖ + ㉚ - ㉞ + ㊳ - ㊷ - ㊻\}, \tag{6j}$$

where the factor i comes from our definition of the interpolation operator for the mesons, e.g. $K^0 = i(\bar{d}\gamma_5 s)$.

A few notes about the contractions shown in Figs. 3–6 may be useful:

(1) The contractions identified by circled numbers do not carry the minus sign required when there is an odd number of fermion loops. Instead, the signs are included explicitly in Eqs. (5) and (6).

(2) The routing of the solid line indicates spin contraction while that of the dashed line indicates the contraction of color indices. If there is no dashed line, then solid line indicates connections implied by the
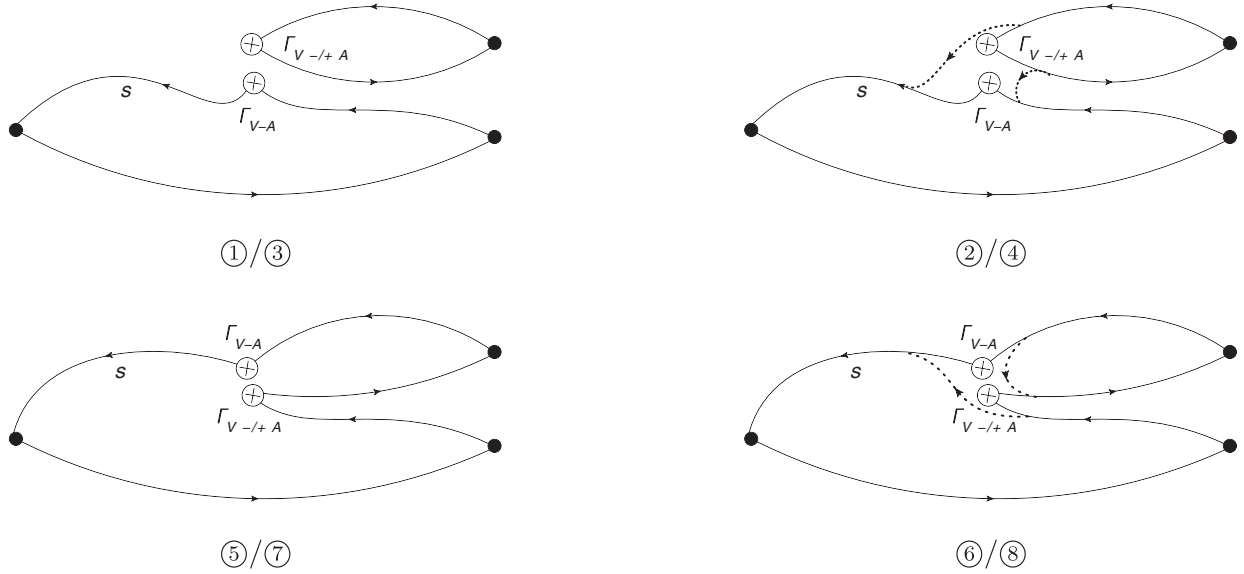
FIG. 3. Diagrams representing the eight $K^0 \to \pi\pi$ contractions of $type1$, where $\Gamma_{V\pm A} = \gamma_\mu(1 \pm \gamma_5)$. The black dot indicates a γ_5 matrix, which is present in each operator creating or destroying a pseudoscalar meson.

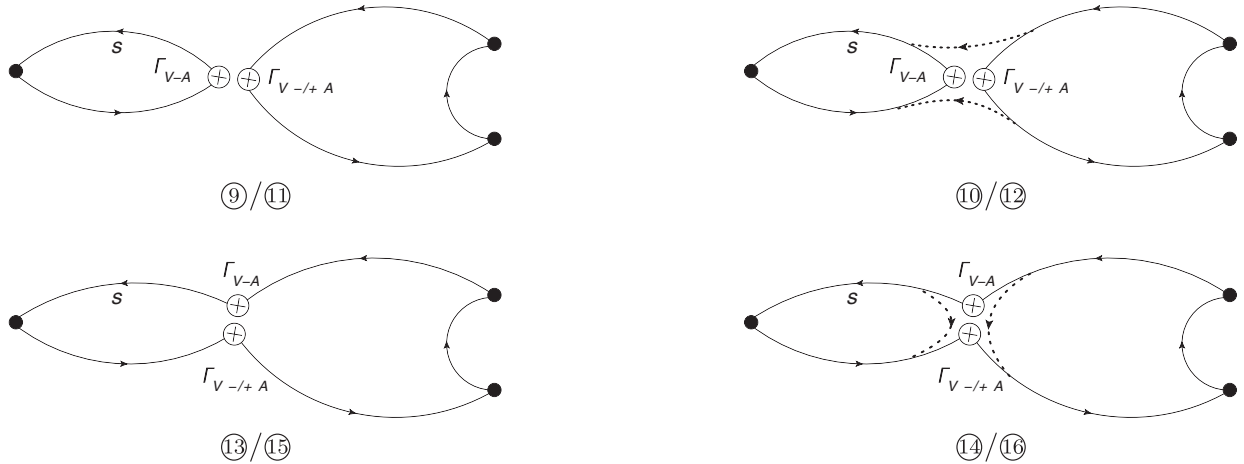

FIG. 4. Diagrams for the eight $type2$ $K^0 \to \pi\pi$ contractions.

trace over both color and spin indices. (This will be explained in more detail below.)

(3) A line represents a light quark propagator if it is not explicitly labeled with 's'. Up and down quarks and particular flavors of pion are not distinguished in Figs. 3–6. Instead, these specific contractions of

strange and light quark propagators are combined in Eqs. (5) and (6) to give the $I = 2$ and $I = 0$ amplitudes directly.

(4) Using Fierz symmetry, it can be shown that there are 12 identities among these contractions:

$$\text{⑥} = -\text{①}, \qquad \text{⑤} = -\text{②}, \qquad \text{⑭} = -\text{⑨}, \qquad \text{⑬} = -\text{⑩}, \tag{7a}$$

$$\text{㉖} = -\text{⑰}, \qquad \text{㉕} = -\text{⑱}, \qquad \text{㉙} = -\text{㉒}, \qquad \text{㉚} = -\text{㉛}, \tag{7b}$$

$$\text{㊷} = -\text{㉝}, \qquad \text{㊶} = -\text{㉞}, \qquad \text{㊺} = -\text{㊳}, \qquad \text{㊻} = -\text{㊲}. \tag{7c}$$

A consequence of these identities is that Eq. (6) is consistent with only seven of the ten operators Q_i being linearly independent and with the three usual relations:

$$Q_{10} - Q_9 = Q_4 - Q_3 \tag{8a}$$

$$Q_4 - Q_3 = Q_2 - Q_1 \tag{8b}$$
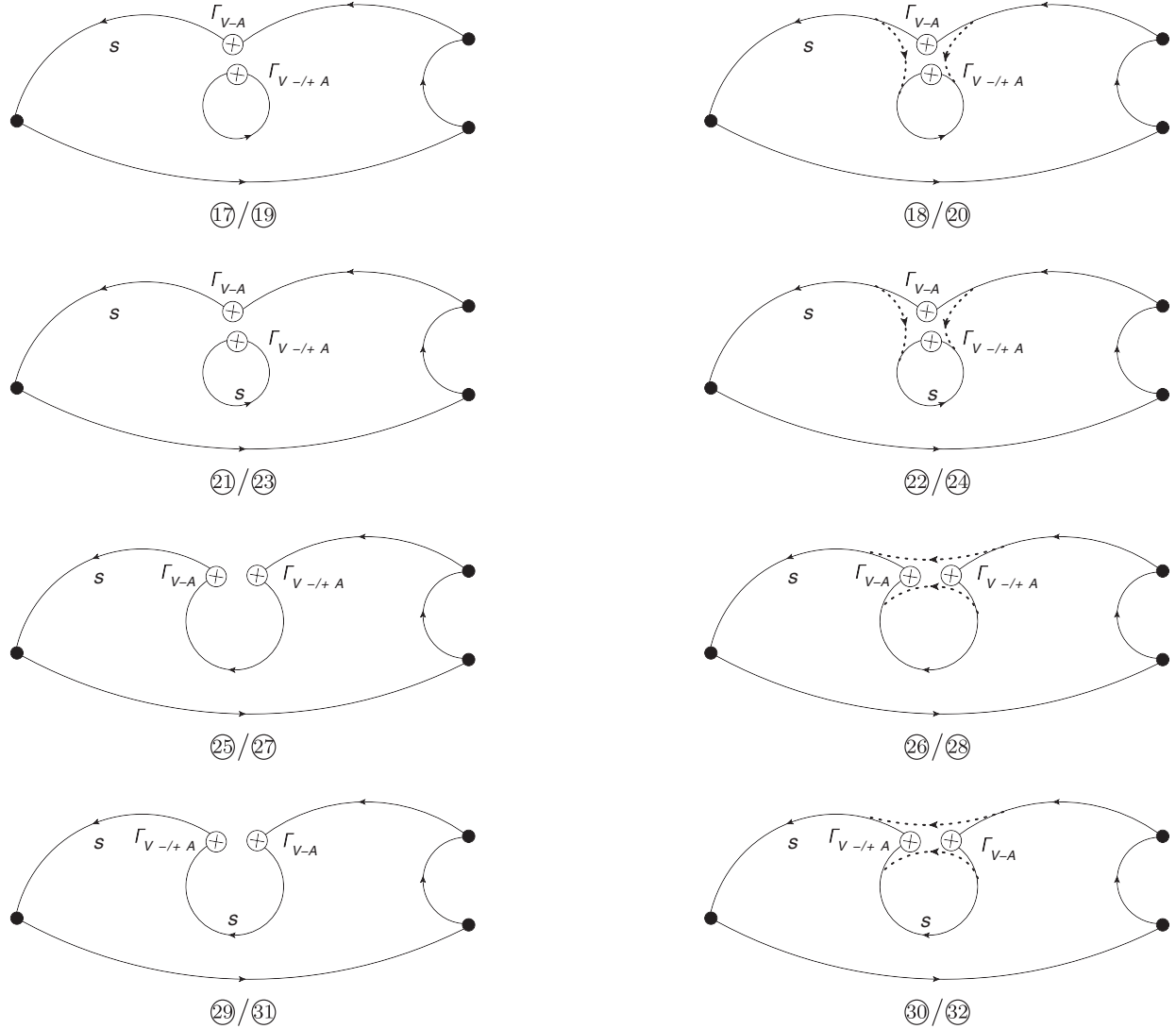
$$2Q_9 = 3Q_1 - Q_3. \tag{8c}$$

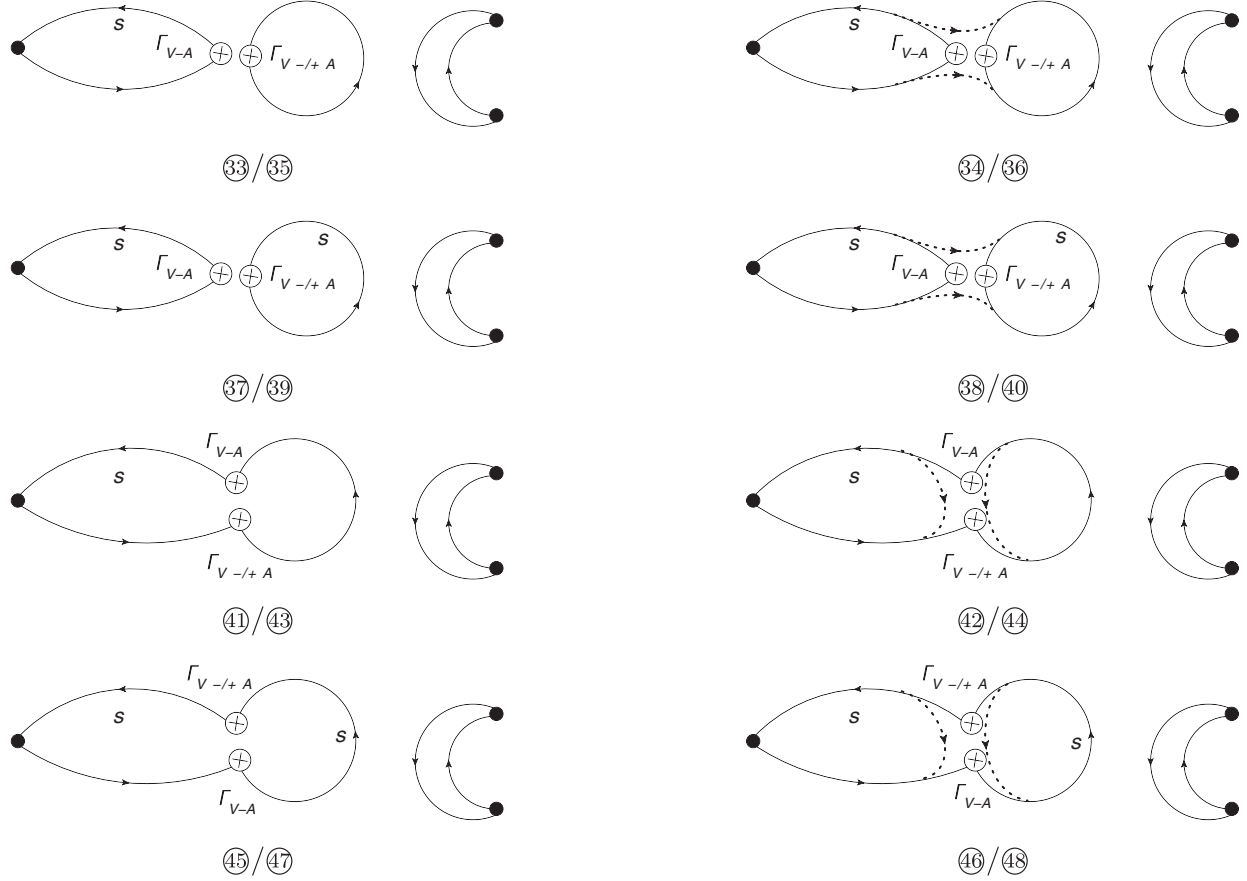FIG. 5.   Diagrams for the 16 *type*3 $K^0 \rightarrow \pi\pi$ contractions.

(5) Based on charge conjugation symmetry and γ^5 hermiticity, the gauge field average of each of these contractions is real.

(6) The loop contractions of *type*3 and *type*4 are calculated using the Gaussian, stochastic wall sources described in Sec. II.

In order to make our approach more explicit, we will discuss some examples. First consider the two contractions of *type*1 identified as ① and ② and shown in the top half of Fig. 3:

$$① = \text{Tr}\{\gamma_\mu(1 - \gamma_5)L(x_{\text{op}}, t_\pi)L(x_{\text{op}}, t_\pi)^\dagger\} \cdot \text{Tr}\Big\{\gamma^\mu(1 - \gamma_5)$$

$$\times L(x_{\text{op}}, t_\pi)\gamma^5\Big[\sum_{\vec{x}_\pi}L((\vec{x}_\pi, t_\pi), t_K)\Big]S(x_{\text{op}}, t_K)^\dagger\Big\} \quad (9)$$

$$② = \text{Tr}_c\Big\{\text{Tr}_s\{\gamma_\mu(1 - \gamma_5)L(x_{\text{op}}, t_\pi)$$

$$\times L(x_{\text{op}}, t_\pi)^\dagger\} \cdot \text{Tr}_s\Big\{\gamma^\mu(1 - \gamma_5)L(x_{\text{op}}, t_\pi)$$

$$\times \gamma_5\Big[\sum_{\vec{x}_\pi}L((\vec{x}_\pi, t_\pi), t_K)\Big]S(x_{\text{op}}, t_K)^\dagger\Big\}\Big\}, \quad (10)$$

where t_K is the time of the kaon wall source, t_π the time at which the two pions are absorbed and $x_{\text{op}} = (\vec{x}_{\text{op}}, t_{\text{op}})$ the location of the weak operator. The function $L(x_{\text{sink}}, t_{\text{src}})$ is the light quark propagator, a 12×12 spin-color matrix, while $S(x_{\text{sink}}, t_{\text{src}})$ is the strange quark propagator. The Hermitian conjugation operation, $\dagger$, operates on these 12×12 matrices. We use Tr_c to indicate a color trace, Tr_s a spin trace, and Tr, with no subscript, stands for both a spin and color trace. We have also used the γ^5 hermiticity of the quark propagators to realize the combination of quark propagators given in Eqs. (9) and (10), allowing both con-

FIG. 6.   Diagrams for the 16 *type*4 $K^0 \to \pi\pi$ contractions.

tractions to be constructed from light and strange propagators computed using Coulomb gauge-fixed wall sources located only at the times t_π and t_K. Note the sum over the spatial components of the sink $\vec{x}_\pi$ creates a symmetrical wall sink provided that the appropriate Coulomb gauge transformation matrix has been applied to the sink color index of this propagator to duplicate the Coulomb gauge-fixed wall source. We will sum over the spatial location, $\vec{x}_{\text{op}}$, of the weak operator, to project onto zero spatial momentum and improve statistics. Below, we will show results as a function of the separations between t_π, t_{op} and t_K.

As a third example, which illustrates the use of random wall sources, consider contraction ⑲ shown in Fig. 5. Using the notation introduced above, this contraction is given by

$$⑲ = \text{Tr}\{\gamma_\mu(1+\gamma_5)L^R(x_{\text{op}}, t_{\text{op}})\}\eta(x_{\text{op}})^* \cdot \text{Tr}\Big\{\gamma^\mu(1-\gamma_5)$$
$$\times L(x_{\text{op}}, t_\pi)\Big[\sum_{\vec{x}'_\pi}L((\vec{x}'_\pi, t_\pi), t_\pi)^\dagger\Big]$$
$$\times \Big[\sum_{\vec{x}_\pi}L((\vec{x}_\pi, t_\pi), t_K)\Big]S(x_{\text{op}}, t_K)^\dagger\Big\}. \qquad (11)$$

Here, $\eta(x)$ is the value of the complex, Gaussian random wall source at the space-time position x, while $L^R(x_{\text{sink}}, t_{\text{src}})$ is the propagator whose source is $\eta(x)\delta(x_0 - t_{\text{src}})$. The Dirac delta function $\delta(x_0 - t_{\text{src}})$ restricts the source to the time plane $t = t_{\text{src}}$. In the usual way, the average over the random source $\eta(\vec{x})$ which accompanies the configuration average, will set to zero all terms in which the source and sink positions for the propagator $L^R(x_{\text{op}}, t_{\text{op}})$ in Eq. (11) differ, giving us the contraction implied by the closed loop in the top left panel of Fig. 5. By using 32 separate propagators each with a random source nonzero on only one of our 32 time slices, we obtain more statistically accurate results than would result from a single random source spread over all times.

An important objective of this calculation is to learn how to accurately evaluate the quark loop integration that is present in *type*3 and *type*4 graphs and which contains a $1/a^2$, quadratically divergent component. As can be recognized from the structure of the diagrams, these divergent terms can be interpreted as arising from the mixing between the dimension-six operators Q_i (for all i but 7 and 8) and a dimension-three "mass" operator of the form $\bar{s}\gamma_5 d$. Such divergent terms are expected and do not represent a breakdown of the standard effective Hamiltonian written in Eq. (4). In fact, given the good chiral symmetry of domain

wall fermions, all other operators with a dimension less than six which might potentially mix with those in Eq. (4) will vanish if the equations of motion are imposed. Therefore, these operators cannot contribute to the Green's functions evaluated in Eqs. (5) and (6) where the operators in H_W are separated in space-time from those operators creating the K meson and destroying the π mesons, a circumstance in which the equations of motion can be applied.

The problematic operator $\bar{s}\gamma_5 d$ is not explicitly removed from the effective Hamiltonian because, again using the equations of motion, $\bar{s}\gamma_5 d$ can be written as the divergence of an axial current and hence will vanish in the physical case where the weak operator H_W carries no four-momentum and is evaluated between on-shell states. While we can explicitly sum the effective Hamiltonian density $\mathcal{H}_W$ over space to ensure H_W carries no spatial momentum, to ensure that no energy is transferred we must arrange that the kaon mass and two-pion energy are equal. We may achieve this condition, at least approximately, but there will be contributions from heavier states, which are normally exponentially suppressed, but which will violate energy conservation and hence will be enhanced by this divergent $\bar{s}\gamma_5 d$ term.

Since $\bar{s}\gamma_5 d$ will not contribute to the physical, energy-conserving $K \to \pi\pi$ amplitude, there is no theoretical requirement that it be removed. The coefficient of this $\bar{s}\gamma_5 d$ piece is both regulator-dependent and irrelevant. The contribution of these terms in a lattice calculation of $K \to \pi\pi$ decay amplitudes will ultimately vanish as the equality of the initial and final energies is made more precise and as increased time separations are achieved. However, the unphysical effects of this $\bar{s}\gamma_5 d$ mixing are much more easily suppressed by reducing the size of this irrelevant term than by dramatically increasing the lattice size and collecting the substantially increased statistics required to work at large time separations.

A direct way to remove this $1/a^2$ enhancement is to explicitly subtract an $\alpha_i \bar{s}\gamma_5 d$ term from each of the relevant operators Q_i where the coefficient α_i can be fixed by imposing the condition

$$\langle 0|Q_i - \alpha_i \bar{s}\gamma_5 d|K\rangle = 0, \tag{12}$$
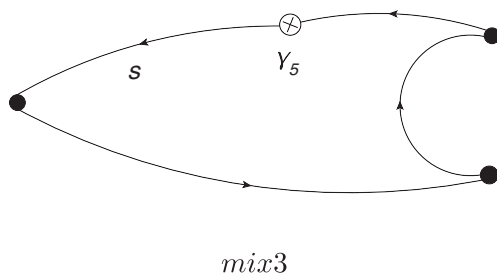
a condition that is typically required in the chiral perturbation theory for $K \to \pi\pi$ [6]. Of course, this arbitrary condition will leave a finite, regulator-dependent $\bar{s}\gamma_5 d$ piece behind in the subtracted operator $Q_i - \alpha_i \bar{s}\gamma_5 d$. However, this unphysical piece will not contribute to the energy-conserving amplitude being evaluated. Since it is no longer $1/a^2$-enhanced, its effects on our calculation will be similar to those of the many other energy nonconserving terms which we must suppress by choosing equal energy K and $\pi\pi$ states and using sufficient large time separation to suppress the contributions of excited states.

Following Eq. (12), we will choose the coefficient α_i from the ratio

$$\alpha_i = \frac{\langle 0|Q_i|K^0\rangle}{\langle 0|\bar{s}\gamma_5 d|K^0\rangle}. \tag{13}$$

(Note, with this definition the coefficient α_i is proportional to the difference of the strange and light quark masses.) Thus, we will improve the accuracy when calculating graphs of $type3$ and $type4$ by including an explicit subtraction term for those operators Q_i where mixing with $\bar{s}\gamma_5 d$ is permitted by the symmetries (all but Q_7 and Q_8):

$$\langle O_0^{\pi\pi}(t_\pi)Q_i(t_{\mathrm{op}})K^0(t_K)\rangle_{\mathrm{sub}}$$
$$= \langle O_0^{\pi\pi}(t_\pi)Q_i(t_{\mathrm{op}})K^0(t_K)\rangle$$
$$- \alpha_i\langle O_0^{\pi\pi}(t_\pi)\bar{s}\gamma_5 d(t_{\mathrm{op}})K^0(t_K)\rangle. \tag{14}$$

We should recognize that there is a second, divergent, parity-even operator $\bar{s}d$ which mixes with our operators Q_i. However, we choose to neglect this effect because parity symmetry prevents it from contributing to either the $K \to \pi\pi$ or $K \to |0\rangle$ correlation functions being evaluated here.

The amplitude $\langle O_0^{\pi\pi}(t_\pi)\bar{s}\gamma_5 d(t_{\mathrm{op}})K^0(t_K)\rangle$ includes two contractions, one connected and one disconnected as shown in Fig. 7. These terms, which arise from the mixing of the operators Q_i with $\bar{s}\gamma_5 d$, are labeled $mix3$ and $mix4$. To better visualize the contributions from different types of contractions, we can write the right-hand side of Eq. (14) symbolically as

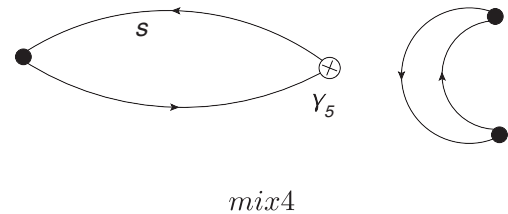$mix3$ $\qquad\qquad\qquad\qquad\qquad\qquad$ $mix4$

FIG. 7. Diagrams showing the contractions needed to evaluate the subtraction terms. These are labeled $mix3$ and $mix4$ and constructed from the $type3$ and $type4$ contractions by replacing the operator Q_i and fermion loop with the vertex $\bar{s}\gamma_5 d$.

$$type1 + type2 + type3 + type4 - \alpha \cdot (mix3 + mix4)$$

$$= type1 + type2 + sub3 + sub4, \qquad (15)$$

where $sub3 = type3 - \alpha \cdot mix3$ and $sub4 = type4 - \alpha \cdot mix4$. Note, here and in later discussions we refer to the term being subtracted as "mix" and the final difference as the subtracted amplitude "sub."

V. $K^0 \to \pi\pi$ $\Delta I = 3/2$ AMPLITUDE

As Eqs. (5) and (7a) show, the $\Delta I = 3/2$ $K^0 \to 2\pi$ decay amplitude includes only $type1$ contractions and four of the correlation functions are related

$$A_{2,10} = A_{2,9} = \frac{3}{2}A_{2,1} = \frac{3}{2}A_{2,2}. \qquad (16)$$

Therefore, we need only to calculate $A_{2,1}$, $A_{2,7}$ and $A_{2,8}$. The corresponding three correlation functions, $C_{2,i}(\Delta, t)$ for $i = 1$, 7 and 8, with the choice of $m_K^{(1)}$ for the kaon mass, are shown in Fig. 8. Here, we exploit our propagator calculation for sources on each of the 32 time slices to compute $C_{2,i}(\Delta, t)$ from an average over all 32 source positions:

$$C_{2,i}(\Delta, t) = \frac{1}{32}\sum_{t'=0}^{31} A_{2,i}(t_\pi = t' + \Delta, t_{op} = t + t', t_K = t').$$
$$\qquad (17)$$

In Fig. 8, we plot $C_{2,i}(\Delta, t)$ for $0 < t < \Delta$ at fixed $\Delta = 12$ or 16. Table I shows that $m_K^{(1)}$ is almost equal to the energy of $I = 2$, $\pi - \pi$ state, so the 3-point correlation function $C_{2,i}(\Delta, t)$ should be approximately independent of t in the central region where the time coordinate of the

operator is far from both the kaon and the two-pion sources, $0 \ll t \ll \Delta$.

We fit the correlators $C_{2,i}(\Delta, t)$ using a single free parameter $M_i^{3/2, \text{lat}}$:

$$C_{2,i}(\Delta, t) = M_i^{3/2, \text{lat}} N_{\pi\pi} N_K e^{-E_{\pi\pi}\Delta} e^{-(m_K - E_{\pi\pi})t}, \qquad (18)$$

where N_K, m_K and $N_{\pi\pi}$, $E_{\pi\pi}$ are determined by fitting the kaon and two-pion correlators respectively:

$$\frac{1}{32}\sum_{t'=0}^{31}\langle K(t+t')K(t')\rangle = N_K^2(e^{-m_K t} + e^{-m_K(T-t)}) \qquad (19)$$

$$\frac{1}{32}\sum_{t'=0}^{31}\langle O_2^{\pi\pi}(t+t')O_2^{\pi\pi}(t')\rangle$$
$$= N_{\pi\pi}^2(e^{-E_{\pi\pi}t} + e^{-E_{\pi\pi}(T-t)} + C). \qquad (20)$$

The constant C arises when the two pions join the source at t' and sink at $t + t'$ by traveling in opposite time directions as discussed below. The fitted results for the matrix elements $M_i^{3/2, \text{lat}}$ from $\Delta = 12$ are listed in Table II in lattice units.

Figure 8 shows that for the operators Q_7 and Q_8 the larger separation, $\Delta = 16$, between the kaon source and $\pi - \pi$ sink gives a much shorter plateau region than the case $\Delta = 12$. This behavior is inconsistent with the usual expectation that it is the contributions from excited states of the kaon and pion, contributions which should be suppressed for larger Δ, that cause the poor plateau. An alternative, consistent explanation attributes the shortened plateau region seen for $\Delta = 16$ to the "around-the-world" effect. This is the contribution to the correlation function in which the two-pion interpolating operator at the sink annihilates one pion and creates another (instead of
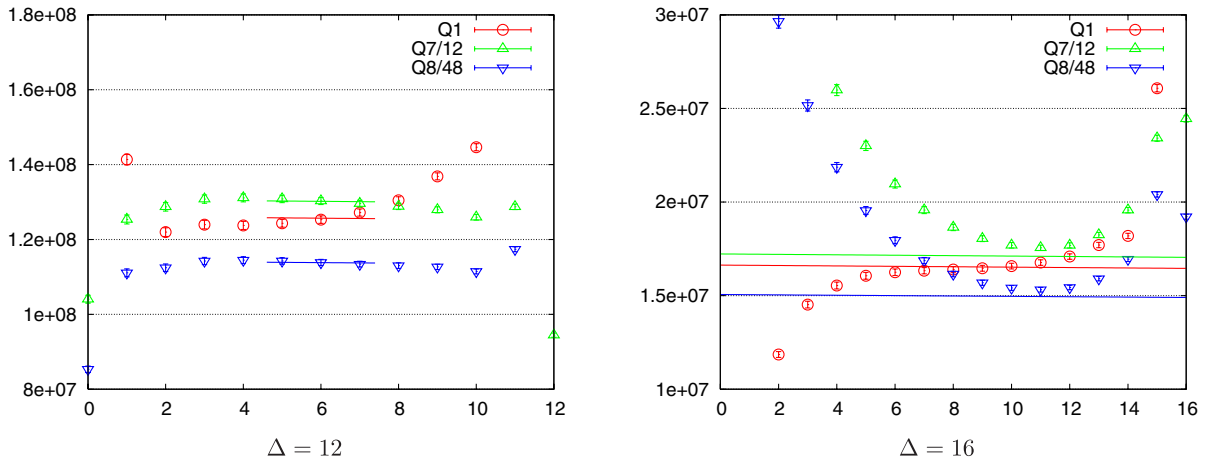
FIG. 8 (color online). Plots of the $\Delta I = 3/2$ $K^0 \to \pi - \pi$ correlation functions for kaon source and $\pi - \pi$ sink separations of $\Delta = 12$ (left panel) and 16 (right panel). The x-axis gives the time t specifying the time slice over which the operator, $Q_i(\vec{x}, t)$, $i = 1, 7,$ 8, is averaged. The results for the operator Q_7 are divided by 12, and those for Q_8 by 48 to allow the results to be shown in the same graph. The correlators $C_{2,i}(\Delta, t)$ are fit using the $\Delta = 12$ data with a fitting range $5 \leq t \leq 7$. The resulting constants are shown as horizontal lines in both the $\Delta = 12$ and 16 graphs. We can see that the $\Delta = 16$ data are consistent with those from $\Delta = 12$, but receive large contributions from the around-the-world paths.

TABLE II. Results for the lattice $\Delta I = 3/2$, $K \to \pi\pi$ transition amplitudes obtained from fitting the 3-point correlation functions to the functional form given in Eq. (18) for the six operators with $\Delta I = 3/2$ components. The second column gives the lattice matrix elements $M_i^{3/2,\mathrm{lat}}(\times 10^{-2})$ while the third and fourth column give their contributions to the real and imaginary parts of A_2.

i	$M_i^{3/2,\mathrm{lat}}(\times 10^{-2})$	Re(A_2)(GeV)	Im(A_2)(GeV)
1	0.4892(16)	$-1.737(11)\mathrm{e}-08$	0
2	$= M_1$	$6.665(42)\mathrm{e}-08$	0
7	6.080(18)	$2.422(16)\mathrm{e}-11$	$4.070(26)\mathrm{e}-14$
8	21.26(6)	$-1.979(13)\mathrm{e}-10$	$-9.646(61)\mathrm{e}-13$
9	$= 1.5M_1$	$-7.917(50)\mathrm{e}-15$	$5.185(24)\mathrm{e}-13$
10	$= 1.5M_1$	$6.103(38)\mathrm{e}-12$	$-1.448(9)\mathrm{e}-13$
Total	-	$4.911(31)\mathrm{e}-08$	$-5.502(40)\mathrm{e}-13$

annihilating two pions as in the $K \to \pi\pi$ contribution we are seeking) and the process at the weak operator is $K\pi \to \pi$ (instead of $K \to \pi\pi$). While one pion travels from the weak operator to the $\pi - \pi$ sink, the second is created at the sink and travels forward in time, passing through the periodic boundary to reach the weak operator together with the kaon. The corresponding dominant path is shown in Fig. 9. The time dependence of this behavior can be estimated as
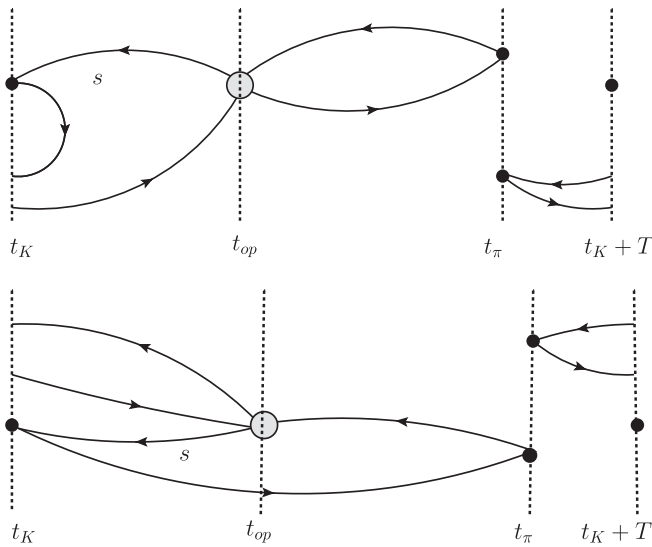

FIG. 9. Diagrams showing the dominant around-the-world paths contributing to graphs of $type\,1$. The space-time region between the kaon wall source at t_K and its periodic recurrence at $t_K + T$ is shown, where $T = 32$ is the extent of the periodic lattice in the time direction. For this around-the-world path, one pion travels directly from the pion wall source at t_π to the weak operator, represented by the grey dot at t_{op}. However, the second pion propagates in the other direction in time, passes through the periodic boundary and combines with the kaon before reaching the weak operator at t_{op}.

$$\sim M_i^{3/2,\mathrm{lat}} N_\pi^2 N_K e^{-m_\pi T} e^{-(E_{K\pi} - m_\pi)t} \qquad (21)$$

which is Δindependent but suppressed by the factor $\exp(-m_\pi T)$, where N_π is the analogue of N_K for the case of single pion production and $T = 32$ is the temporal extent of the lattice. In contrast, the physical contribution in Eq. (18) is suppressed by $\exp(-E_{\pi\pi}\Delta)$. Thus, the second, standard term falls with increasing Δ and the two factors are of similar size when $\Delta = T/2$. Therefore, we should expect to see a large contamination from such around-the-world effects in the $\Delta = 16$ case, consistent with Fig. 8. In both panels of that figure, we plot as three horizontal lines the fitted result from $\Delta = 12$ for the three amplitudes $M_i^{3/2,\mathrm{lat}} N_{\pi\pi} N_K \exp-(\Delta E_{\pi\pi})$ for $i = 1, 7$ and 8. The agreement between these lines and the short plateaus seen in the right-hand, $\Delta = 16$ panel indicates consistency between these two values of Δ.

Additional evidence supporting this explanation for the short plateau in the case of $\Delta = 16$ can be obtained by examining the explicit dependence on t given by Eq. (21) for the around-the-world contribution. Examining the exponential decay with t in the $\Delta = 16$ correlators plotted in the right panel of Fig. 8, for operators Q_7 and Q_8 we find a value for $E_{K\pi} - m_\pi$ varying between 0.4 and 0.5 depending on the choice of fit range. A more accurate value of 0.498(2) can be obtained by fitting the corresponding correlator for $\Delta = 20$ and a fit range of 5 to 11. The strangeness-carrying state whose mass we have labeled $E_{K\pi}$ can be formed from two quarks and must be parity-even. Direct calculation of $E_{K\pi}$ from a scalar $\bar{s}d$ correlator yields $E_{K\pi} = 0.752(12)$ which is consistent with the sum of the result above, $E_{K\pi} - m_\pi = 0.498(2)$, and the pion mass $m_\pi = 0.2437(5)$. (This energy difference is also close to the kaon mass $m_K^{(1)} = 0.50729$ given in Table I.) Thus, the time dependence expected from the around-the-world path is quite consistent with that seen in Fig. 8.

We conclude that it is important to increase the lattice extent in the time direction both to suppress this around-the-world effect and to permit the use of a larger source-sink separation giving a longer plateau. We will return to discussion of the around-the-world effect below for the $\Delta I = 1/2$ kaon decay where it creates even greater difficulties. However, here we can begin to appreciate the severity of this effect in the $K^0 \to \pi\pi$ system for our temporal lattice extent of 32, given our values of the lattice spacing and meson masses.

The Wilson coefficients and operators which appear in Eq. (4) are typically expressed in the $\overline{\mathrm{MS}}$ scheme. Thus, we must change the normalization of our lattice operators Q_i to that of the $\overline{\mathrm{MS}}$ scheme. We begin by converting our bare lattice operators into the regularization invariant momentum (RI/MOM) scheme of Ref. [15]. Here, we use the earlier results of Ref. [26] which were obtained for the present lattice action using the methods of Ref. [6]. In this previous work off-shell, Landau-gauge-fixed Green's

functions containing the lattice operators Q_i are evaluated at specific external momenta characterized by an energy scale μ. These results determine a renormalization matrix $Z_{ij}^{RI}(\mu, a)$ which can be used to convert the lattice normalization into that of the RI scheme:

$$Q^{RI}(\mu)_i = \sum_{j=1}^{7} Z_{ij}^{lat \to RI}(\mu, a) Q'_j. \qquad (22)$$

As explained in Appendix A, these equalities hold only when the operators appear in physical matrix elements. The indices i and j take on seven values corresponding to the seven independent operators in what will be called the chiral basis. (The primes in this equation indicate lattice operators defined in that basis.) This is referred to as nonperturbative renormalization because the matrix $Z_{ij}^{lat \to RI}(\mu, a)$ is computed using a lattice evaluation of off-shell Green's functions and perturbation theory is not used.

Next, these $Q^{RI}(\mu)_i$ operators are converted to the $\overline{MS}$ scheme in which the Wilson coefficients are evaluated by applying a conversion matrix $R_{ij}^{RI \to \overline{MS}}$ discussed in detail in Ref. [16]. Finally, the matrix elements of these $\overline{MS}$ operators are combined with the Wilson coefficients obtained in the $\overline{MS}$ scheme [17] using the scale $\mu = 2.15$ GeV to determine the results given later in this section for the $\Delta I = 3/2$ amplitude A_2 and in the following section for the $\Delta I = 1/2$ A_0. These procedures are described in greater detail in Appendix A.

A good approximation to the infinite volume decay amplitude can be obtained by including the Lellouch-Lüscher factor (F) [18] which relates the $K \to \pi\pi$ matrix element M of the effective weak Hamiltonian of Eq. (4) calculated using finite volume states normalized to unity to the infinite volume amplitude A: $|A|^2 = F^2 M^2$ where

$$F^2 = 4\pi \left(\frac{E_{\pi\pi}^2 m_K}{p^3}\right) \left\{ p \frac{\partial \delta_2(p)}{\partial p} + q \frac{\partial \phi(q)}{\partial q} \right\}. \qquad (23)$$

Here, p is defined through $E_{\pi\pi} = 2\sqrt{m_\pi^2 + p^2}$, $q = Lp/2\pi$ and $\delta_2(p)$ is the s-wave, $I = 2$, $\pi - \pi$ scattering phase shift for pion relative momentum p. The function $\phi(q)$ is known analytically and given, for example, in Ref. [18]. The $I = 2$ phase shift $\delta_2(p)$ is determined from the measured two-pion energy $E_{\pi\pi} = 0.443(13)$ given in Table I and the finite volume quantization condition [27]

$$\phi(q) + \delta_2(p) = n\pi. \qquad (24)$$

For our threshold case, we set the integer n to zero and obtain $\delta_2(p) = -0.0849(43)$. Because of the small value of p, we assume that $\delta_2(p)$ is a linear homogenous function of p and write $\delta_2(p) = p \partial \delta_2(p)/\partial p$, the quantity required in Eq. (23) and given in Table III. (Equation (23) differs by a factor of 2 from the expression given in the

TABLE III. The calculated quantities which appear in the Lellouch-Lüscher factor F for $I = 2$. The corresponding factor for the case of noninteracting particles is $F_{free} = 31.42$. The difference reflects the final two-pion scattering in a box.

p	$q\frac{\partial\phi(q)}{\partial q}$	$p\frac{\partial\delta(p)}{\partial p}$	F
0.0690(13)	0.221(10)	$-0.0849(43)$	26.01(18)

Lellouch-Lüscher paper because of our different conventions for the decay amplitude A. With our conventions, the experimental value of $\text{Re}(A_2) = 1.48 \times 10^{-8}$ GeV.)

In the limit of noninteracting pions, the factor F becomes $F_{free}^2 = 2(2m_\pi)^2 m_K L^3$, which reflects the different normalization of states in a box and plane wave states in infinite-volume. Results for F in this $I = 2$ case and the quantities used to determine it are given in Table III. We should note that applying the finite-volume correction of Eq. (23) gives us a finite-volume corrected amplitude for a $\Delta I = 3/2$, $K \to \pi\pi$ decay that is slightly above threshold by the amount $E_2^{\pi\pi} - 2m_\pi = 33(1)$ MeV.

We can now combine everything and calculate the $K^0 \to \pi\pi$ decay amplitudes,

$$A_{2/0} = F \frac{G_F}{\sqrt{2}} V_{ud} V_{us} \sum_{i=1}^{10} \sum_{j=1}^{7} [(z_i(\mu)$$
$$+ \tau y_i(\mu)) Z_{ij}^{lat \to \overline{MS}} M_j^{(3/2)/(1/2),lat}], \qquad (25)$$

where the construction of the 10×7 renormalization matrix $Z_{ij}^{lat \to \overline{MS}}$ is explained in Appendix A. For later use, we have written Eq. (25) in a way which is applicable for $\Delta I = 1/2$ decays as well as for the $\Delta I = 3/2$ transitions considered in this section. The results for the complex $\Delta I = 3/2$ decay amplitude A_2 are summarized in Table IV, including those for the other two, energy-non-conserving choices of kaon mass. Since $m_K^{(1)}$ differs from the isospin-2 $\pi - \pi$ energy by only 0.2%, we quote this case as our energy-conserving kaon decay amplitude. Therefore, in physical units, we obtain the energy-conserving $\Delta I = 3/2$, $K^0 \to \pi\pi$ complex, threshold decay amplitude for $m_K = 877$ MeV and $m_\pi = 422$ MeV:

$$\text{Re}(A_2) = 4.911(31) \times 10^{-8} \text{ GeV} \qquad (26)$$

$$\text{Im}(A_2) = -0.5502(40) \times 10^{-12} \text{ GeV}. \qquad (27)$$

TABLE IV. The complex, $K^0 \to \pi\pi$, $\Delta I = 3/2$ decay amplitudes in units of GeV.

m_K	$\text{Re}(A_2)(\times 10^{-8})$	$\text{Im}(A_2)(\times 10^{-12})$
$m_K^{(0)}$	4.308(28)	$-0.5596(40)$
$m_K^{(1)}$	4.911(31)	$-0.5502(40)$
$m_K^{(2)}$	5.916(38)	$-0.5316(39)$

This result for Re(A_2) can be compared with the experimental value of 1.48×10^{-8} GeV given above. The larger result found in our calculation is likely explained by our unphysically heavy kaon and pions.

VI. $K^0 \to \pi\pi$ $\Delta I = 1/2$ AMPLITUDE

Following the prescription given by Eq. (6), we have calculated all of the $\Delta I = 1/2$ kaon decay correlation functions,

$$C_{0,i}(\Delta, t) = \frac{1}{32} \sum_{t'=0}^{31} A_{0,i}(t_\pi = t' + \Delta, t_{\rm op} = t + t', t_K = t'),$$

(28)

for each of the 10 effective weak operators. In the calculation, we treat each of these 10 operators as independent and then verify that the identities shown in Eq. (8) are automatically satisfied. Figs. 10 and 11 show two examples of the resulting correlation functions for the operators Q_2

and Q_6, in the case of the lightest kaon $m_K^{(0)}$. Table I shows that the mass of this kaon is very close to the energy of the $I = 0$ two-pion state. Therefore, we expect to get a reasonably flat plateau when the operator is far from both the source and sink.

Given this good agreement between the energies of the K and $\pi - \pi$ states, we might expect that the unphysical, dimension-three operator, $\bar{s}\gamma^5 d$ which mixes with the (8, 1) operators in Eq. (4) and is itself a total divergence, will also give a negligible contribution to such an energy and momentum-conserving matrix element. However, as can be seen from Figs. 10(a) and 11(a), the matrix element of this term is large and the explicit subtraction described in Sec. IV is necessary.

This difficulty is created by the combination of two phenomena. First, the mixing coefficient which multiplies the $\bar{s}\gamma^5 d$ operator when it appears in our weak (8, 1) operators is large, of order $(m_s - m_l)/a^2$. Second, in our lattice calculation the necessary energy-conserving kinematics (needed to insure that this total divergence does not
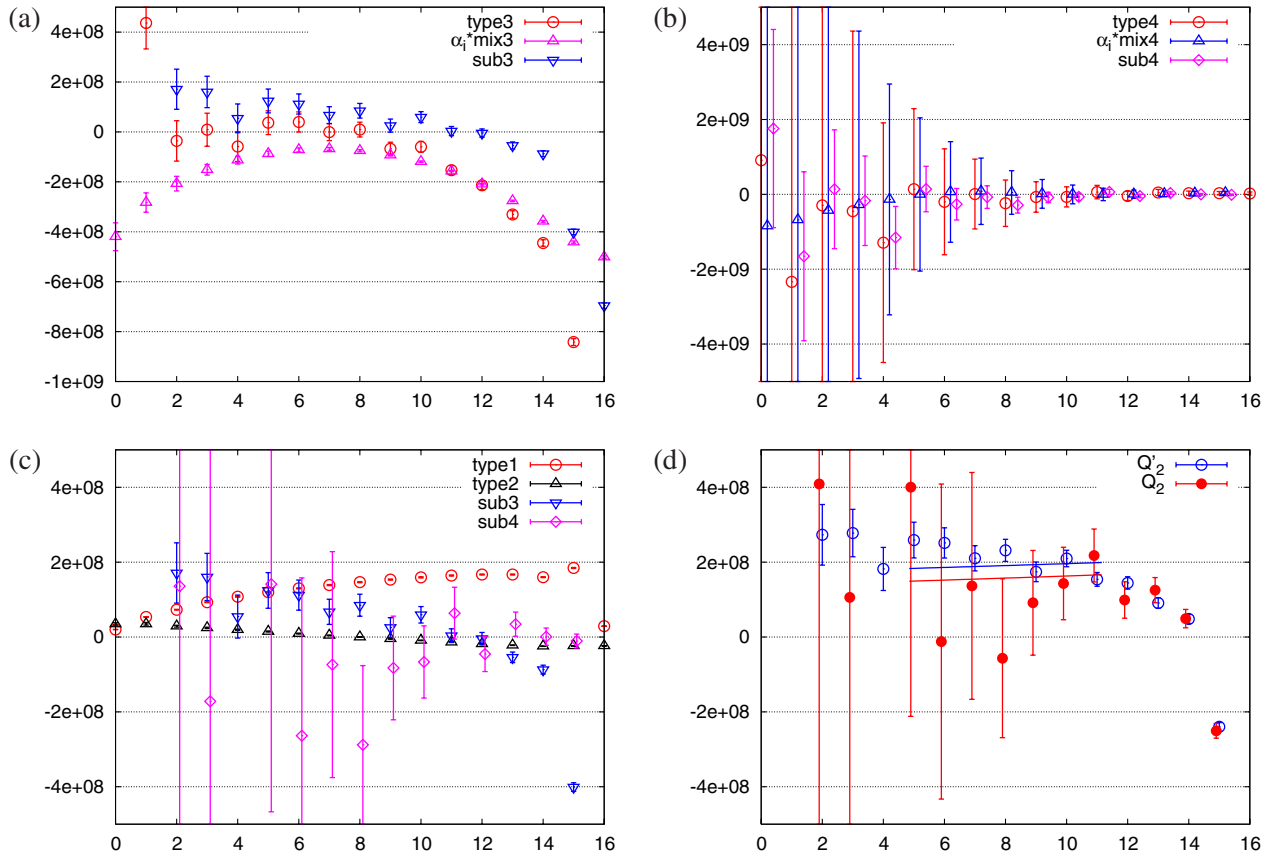
FIG. 10 (color online). Plots showing the t dependence of the various contractions which contribute to the $\Delta I = 1/2$ correlation function $C_{0,2}(\Delta = 16, t)$ for the operator Q_2. (a) Contractions of $type3$, the divergent mixing term $mix3$ that will be subtracted and the result after subtraction, $sub3$. (b) Contractions of $type4$, the divergent mixing term $mix4$ that will be subtracted and the result after subtraction, $sub4$. (c) Results for each of the four types of contraction after the needed subtractions have been performed. (d): Results for the complete Q_2 correlation function $C_{0,2}(\Delta = 16, t)$ obtained by combining these four types of contractions. The solid points labeled Q_2 are the physical result while the open points labeled Q_2' are obtained by omitting all the vacuum graphs, $sub4$. The solid and dotted horizontal lines indicate the corresponding fitting results and the time interval, $5 \le t \le 11$ over which the fits are performed.
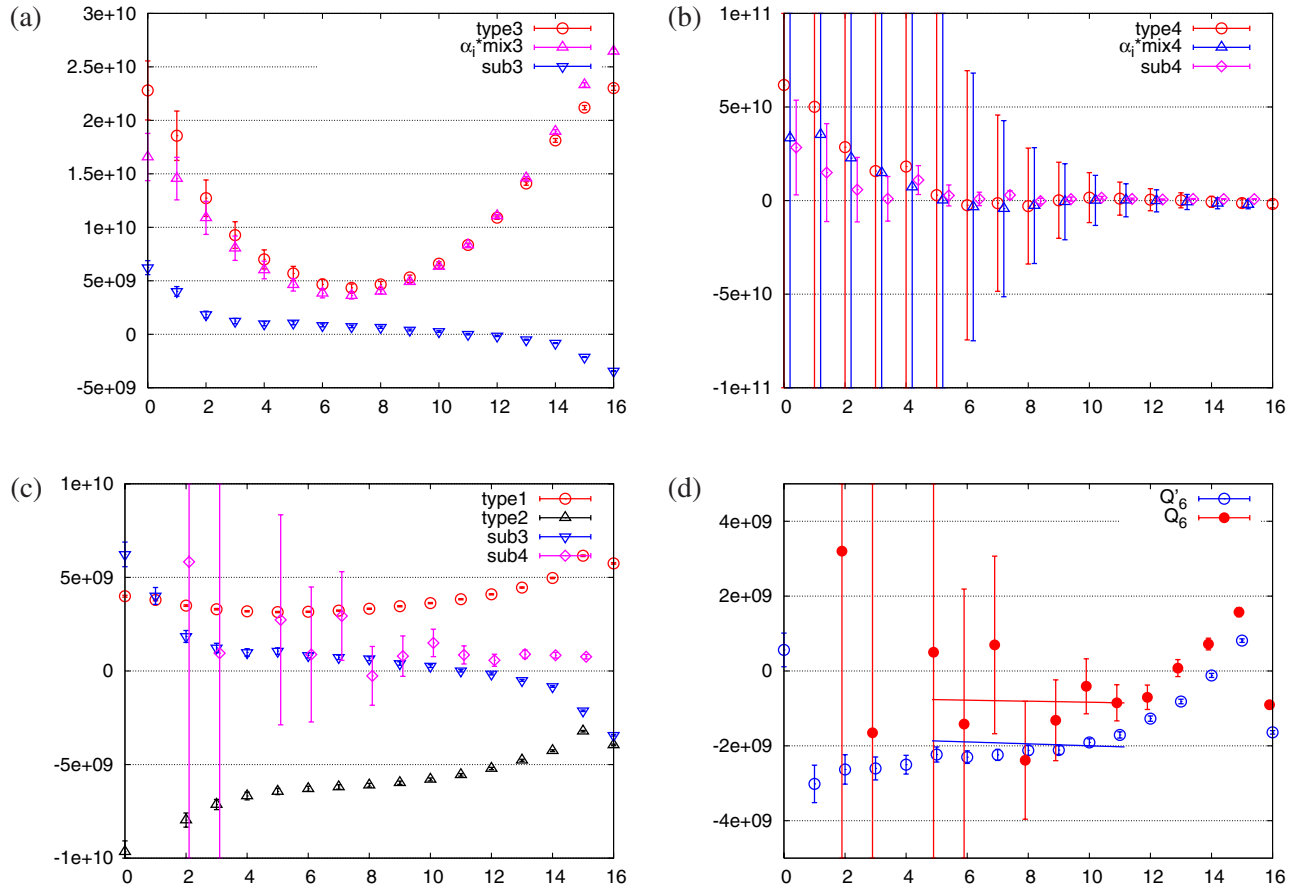
FIG. 11 (color online).   The result for each type of contraction contributing to the 3-point correlation function $C_{0,6}(\Delta = 16, t)$ for the operator Q_6 following the same conventions as in Fig. 10.

contribute) is only approximately valid. The required equality of the spatial momenta of the kaon and $\pi - \pi$ states is assured by our summing the location of the weak vertex over a complete temporal hyperplane. On the other hand, the equality of the energies of the initial and final states results only if we have adjusted the kaon mass to approximately that of the two-pion state and chosen the time extents sufficiently large that other states with different energies have been suppressed. However, as can be seen in Figs. 10(a) and 11(a) the subtraction terms $mix3$ and $mix4$ show strong dependence on the time at which they are evaluated. This implies that there are important contributions coming from initial and final states which have significantly different energies. One or both of these states is then not the intended K or $\pi - \pi$ state but instead an unwanted contribution which has been insufficiently suppressed by the time separations between source, weak operator and sink.

Thus, instead of relying on large time extents and energy-conserving kinematics to suppress this unphysical, $O(1/a^2)$ term we must explicitly remove it. As explained in Sec. IV, this can be done by including an explicit subtraction which we fix by the requirement that the

kaon to vacuum matrix element of the complete subtracted operator vanishes as in Eq. (12). Thus, we determine the divergent coefficient of this mixing term from the ratio $\alpha_i = \langle 0|Q_i|K\rangle / \langle 0|\bar{s}\gamma^5 d|K\rangle$ and then perform the explicit subtraction of the resulting terms, labeled $\alpha_i \cdot mix3$ and $\alpha_i \cdot mix4$ in Figs. 10 and 11.

Of course, the finite part of such a subtraction is not determined from first principles and our choice, specified by Eq. (12) is arbitrary. Thus, we must rely on our identification of a plateau and the approximate energy conservation of our kinematics to make the arbitrary part of this subtraction small, along with the other errors associated with evaluating the decay matrix element of interest between initial and final states with slightly different energies.

We now examine the very visible time dependence in Figs. 10(a) and 11(a) for both the original matrix elements and the subtraction terms in greater detail. As discussed above, one might expect these divergent subtraction terms to contribute to excited state matrix elements in which the energies of the initial and final states are very different. Typical terms should be exponentially suppressed as the separation between the weak operator and the source or

sink is increased, with the time behavior $\exp\{-(m_K^* - m_K)t\}$ or $\exp\{-(E_{\pi\pi}^* - E_{\pi\pi})(\Delta - t)\}$, whichever is larger. (The $*$ denotes an excited state.) However, by carefully examining the time behavior of the *mix*3 amplitude, we find that the time dependence, at least in the vicinity of the central region, is less rapid than might be expected from such excited states suggesting that it is probably not due primarily to contamination from excited states.

We believe that the dominant, energy-nonconserving matrix elements which cause the significant time dependence in Figs. 10 and 11 arise from the around-the-world effects identified and discussed in the previous $\Delta I = 3/2$ section. In fact, for the reasons just discussed associated with divergent operator mixing, such around-the-world effects are a more serious problem in the $\Delta I = 1/2$ case. The dominant around-the-world graphs are shown in Fig. 12. An estimate of the time dependence of these graphs gives,

FIG. 12. The dominant around-the-world paths contributing to graphs of *type*3. As in Fig. 9 we show the space-time region between the kaon source at $t = t_K$ and its periodic recurrence at $t = t_K + T$. The gray circle represents the four-quark operator Q_i. For the first two graphs, one of the two pions created at the $t = t_\pi$ source travels directly to the operator Q_i while the second pion travels in the other direction in time and reaches the kaon and weak operator by passing through the periodic lattice boundary. In the third diagram, it is the kaon which travels in the opposite to the expected time direction.

$$< K^0\pi|Q_i|\pi > N_\pi N_K N_\pi e^{-m_\pi T} e^{-(E_{K\pi}-m_\pi)t}$$
$$+ <0|Q_i|K^0\pi\pi > N_\pi N_K N_\pi e^{-m_K((T-\Delta)+(\Delta-t))}, \quad (29)$$

where the first term comes from the first two graphs of Fig. 12, while the second term comes from the third graph. (Recall that $t = t_{op} - t_K$ and $\Delta = t_\pi - t_K$.) Notice that these two terms involve amplitudes which are far from energy conserving and therefore contain large divergent contributions from mixing with the operator $\bar{s}\gamma_5 d$ which will be removed only when combined with the corresponding around-the-world paths occurring in the *mix*3 contraction.

We conclude that it is these around-the-world matrix elements which are the reason for the observed large divergent subtraction in the *type*3 graph. The largest divergent contribution is thus not the subtraction for the matrix element we are trying to evaluate, $<\pi\pi|Q_i|K^0>$; rather, it is the divergent subtraction for the matrix elements $<K^0\pi|Q_i|\pi>$ and $<0|Q_i|K^0\pi\pi>$ which arise from the around-the-world paths which are not sufficiently suppressed by our lattice size. Two important lessons can be learned from this analysis. First, it is important to perform an explicit subtraction of the divergent mixing with the operator $\bar{s}\gamma_5 d$. While this term will not contribute to the energy-conserving matrix element of interest, in a Euclidean space lattice calculation there are in general, other, unwanted, energy nonconserving terms which may be uncomfortably large if this subtraction is not performed. Second it would be wise to work on a lattice with a much larger size T in time direction in order to suppress further the around-the-world terms which give such a large contribution in the present calculation. Using the average of propagators computed with periodic plus antiperiodic boundary conditions to effectively double the length in the time direction would be a good solution.

We should emphasize that these divergent, around-the-world contributions do not pose a fundamental difficulty. The largest part of these amplitudes are removed by the corresponding subtraction terms constructed from the operator $\bar{s}\gamma_5 d$. The remaining finite contributions from this and other around-the-world terms are suppressed by the factor $\exp(-m_\pi T)$ or $\exp(-m_K(T - \Delta))$. Fortunately, the large divergent subtraction also reduces the statistical errors substantially, especially for the *type*4 vacuum graphs, which indicates the expected strong correlation between the divergent part of the weak operator and the corresponding $\bar{s}\gamma_5 d$ subtraction. Our results suggest that the separation of $\Delta = 16$ gives a relatively longer plateau region, so we use that $K - \pi\pi$ time separation in the analysis below.

The lattice matrix elements are determined by fitting the $I = 1/2$ correlators $C_0^i(\Delta, t)$ given in Eq. (28) using the fitting form:

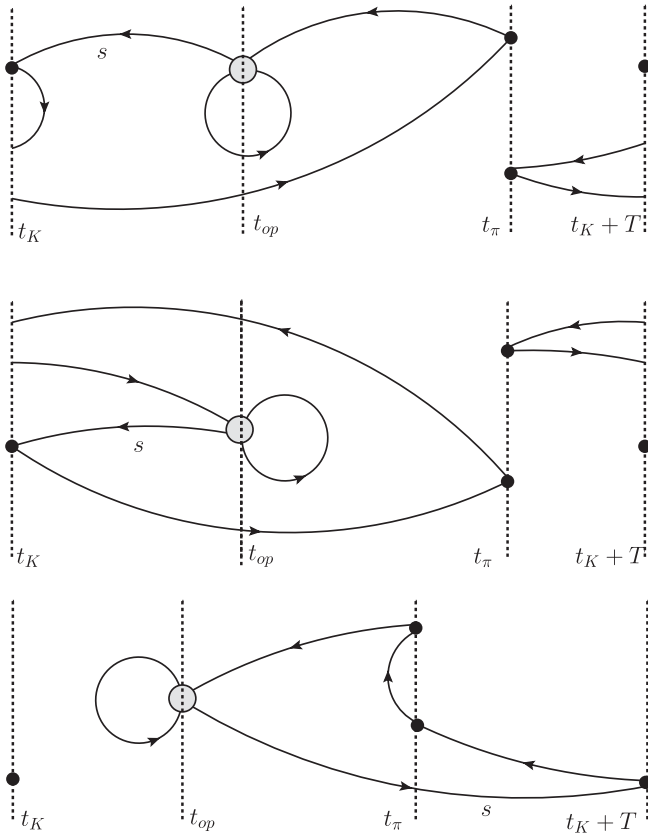$$C_{0,i}(\Delta, t) = M_i^{1/2,\text{lat}} N_{\pi\pi} N_K e^{-E_{\pi\pi}\Delta} e^{-(m_K-E_{\pi\pi})t}. \quad (30)$$

The fitted results for the weak, $\Delta I = 1/2$ matrix elements of all 10 operators are summarized in Table V. To see the effects of the disconnected graph clearly, a second fit is performed to the amplitude from which the disconnected, $type4$ graphs have been omitted and the calculated results are shown with an additional $'$ label, as in the earlier two-pion scattering section.

The calculation of the $\Delta I = 1/2$ decay amplitude A_0 from the lattice matrix elements $M_i^{1/2,\text{lat}}$ given in Table V is very similar to the $\Delta I = 3/2$ case: the values of $M_i^{1/2,\text{lat}}$ are simply substituted in Eq. (25). However, the attractive character of the $I = 0$, $\pi - \pi$ interaction and resulting negative value of p^2 makes the Lellouch-Lüscher treatment of finite volume corrections inapplicable. For the repulsive $I = 2$ case, we could apply this treatment to obtain the decay amplitude for a two-pion final state which was slightly above threshold corresponding to the actual finite volume kinematics. In the present case, there is no corresponding infinite-volume decay into two pions below threshold and an unphysical increase of m_π to compensate for the finite-volume $\pi - \pi$ attraction will introduce an $O(1/L^3)$ error in the decay amplitude of the same size as

that which the Lellouch-Lüscher treatment corrects. Thus, for this $\Delta I = 1/2$ we do not include finite volume corrections and simply use the free-field value for the factor F in Eq. (25).

While we believe that we cannot consistently apply the Lellouch-Lüscher finite volume correction factor to improve our result for the $I = 0$, $K \to \pi\pi$ decay amplitude, we might still be able to use the quantization condition of Eq. (24) to determine the $I = 0$ $\pi - \pi$ scattering phase shift $\delta_0(p)$. Even though Eq. (24) can be analytically continued to imaginary values of the momentum p, its application for large negative p^2 is uncertain since the function $\phi(q)$ becomes ill defined. In fact, our value of p^2 sits very close to a singular point of $\phi(q)$. We believe this happens because the condition on the interaction range $R \ll L/2$ used to derive the quantization condition in Eq. (24) is not well satisfied for our small volume. This impediment to determining $\delta_0(p)$ will naturally disappear once we work with lighter pions in a larger volume.

The results for Re(A_0) and Im(A_0) are summarized in Table VI and the individual contribution from each of the operators is detailed in the last two columns of Table V. Within a large uncertainty Table V shows that the largest

TABLE V. Fitted results for the weak, $\Delta I = 1/2$ kaon decay matrix elements using the kaon mass $m_K^{(0)}$. The column M_i^{lat} shows the complete result from each operator. The column $M_i'^{\text{lat}}$ shows the result when the disconnected graphs are omitted while the 4th and 5th columns show the contributions of each operator the real and imaginary parts of the physical decay amplitude A_0. These results are obtained using a source-sink separation $\Delta = 16$, and a fit range $5 \leq t \leq 11$.

i	$M_i^{1/2,\text{lat}}(\times 10^{-2})$	$M_i'^{1/2,\text{lat}}(\times 10^{-2})$	Re(A_0)(GeV)	Im(A_0)(GeV)
1	$-1.6(16)$	$-1.10(37)$	$7.6(64)\text{e} - 08$	0
2	$1.52(61)$	$1.92(15)$	$2.86(97)\text{e} - 07$	0
3	$-0.3(41)$	$0.3(10)$	$2.1(136)\text{e} - 10$	$1.1(76)\text{e} - 12$
4	$2.7(33)$	$3.32(78)$	$4.2(44)\text{e} - 09$	$1.4(14)\text{e} - 11$
5	$-3.3(38)$	$-6.81(86)$	$3.1(53)\text{e} - 10$	$1.6(28)\text{e} - 12$
6	$-7.8(48)$	$-19.6(9)$	$-5.6(33)\text{e} - 09$	$-3.3(20)\text{e} - 11$
7	$10.9(14)$	$15.20(42)$	$5.2(12)\text{e} - 11$	$8.8(20)\text{e} - 14$
8	$35.7(28)$	$47.2(10)$	$-3.66(28)\text{e} - 10$	$-1.79(14)\text{e} - 12$
9	$-2.2(12)$	$-1.79(29)$	$3.1(15)\text{e} - 14$	$-2.01(96)\text{e} - 12$
10	$0.9(12)$	$1.24(29)$	$1.2(11)\text{e} - 11$	$-2.7(27)\text{e} - 13$
Total	-	-	$3.46(78)\text{e} - 07$	$-2.4(23)\text{e} - 11$

TABLE VI. Amplitudes for $\Delta I = 1/2$ $K^0 \to \pi\pi$ decay in units of GeV. The energy-conserving amplitudes are obtained by a simple linear interpolation between $m_K^{(0)} = 0.42599$ and $m_K^{(1)} = 0.50729$ to the energy of two-pion state. As in the previous tables, the $'$ indicates results from which the disconnected graphs have been omitted.

m_K	Re(A_0)($\times 10^{-8}$)	Re(A_0')($\times 10^{-8}$)	Im(A_0)($\times 10^{-12}$)	Im(A_0')($\times 10^{-12}$)
$m_K(0)$	$36.1(78)$	$42.3(20)$	$-21(21)$	$-66.1(43)$
$m_K(1)$	$45(10)$	$48.8(24)$	$-41(26)$	$-74.6(47)$
$m_K(2)$	$65(15)$	$58.6(32)$	$-69(39)$	$-89.6(63)$
Energy conserving	$38.0(82)$	$43.4(21)$	$-25(22)$	$-67.5(44)$

contribution to Re(A_0) comes from operator Q_2, and that to Im(A_0) from Q_6 as found, for example, in Refs. [6,7].

Since the choice $m_K^{(0)}$ for the kaon mass is not precisely equal to the energy of the $I = 0$ $\pi\pi$ state, we carried out a simple linear interpolation between $m_K^{(0)}$ and $m_K^{(1)}$ to obtain an energy-conserving matrix element, which is shown in the last row of Table VI. In terms of physical units, therefore, our full calculation gives the energy-conserving, $K^0 \to \pi\pi$, $\Delta I = 1/2$, complex decay amplitude A_0 for $m_K = 766$ MeV and $m_\pi = 422$ MeV:

$$\mathrm{Re}\,(A_0) = 3.80(82) \times 10^{-7}\ \mathrm{GeV} \tag{31}$$

$$\mathrm{Im}\,(A_0) = -2.5(2.2) \times 10^{-11}\ \mathrm{GeV}. \tag{32}$$

These complete results can be compared with those obtained when the disconnected graphs are neglected given in Table VI and the experimental value for Re(A_0) = 3.3×10^{-7} GeV.

VII. DISCUSSION AND CONCLUSIONS

Comparing the results of Re(A_2) in Table IV and Re(A_0) in Table VI, we find the $\Delta I = 1/2$ enhancement ratio Re(A_0)/Re(A_2) to be roughly 7–9. This comparison is degraded by our threshold kinematics which, since the $I = 0$ and $I = 2$ two-pion states have different energies in a finite volume, causes us to use a different kaon mass in the calculations of (A_2) and (A_0) in order to have energy-conserving decays in each case. These two energy-conserving amplitudes have a ratio of $38.0/4.911 = 7.7$, while if we ignore energy conservation and use the same $m_K^{(1)}$ value for kaon mass, the ratio becomes $45.0/4.911 = 9.2$. Of course, both estimates are far from the experimental ratio of 22.5, suggesting that our 422 MeV pion mass and small lattice volume are far from physical.

For completeness, we also calculate the measure of direct CP violation,

$$\mathrm{Re}\left(\frac{\epsilon'}{\epsilon}\right) = \frac{\omega}{\sqrt{2}|\epsilon|}\left[\frac{\mathrm{Im}(A_2)}{\mathrm{Re}(A_2)} - \frac{\mathrm{Im}(A_0)}{\mathrm{Re}(A_0)}\right], \tag{33}$$

where $\omega = \mathrm{Re}(A_2)/\mathrm{Re}(A_0)$ is the inverse of the $\Delta I = 1/2$ enhancement factor. Using our kinematics, the kaon mass $m_K^{(1)}$ and substituting the experimental value for ϵ, we get Re(ϵ'/ϵ) = $(2.7 \pm 2.6) \times 10^{-3}$. If we instead use the experimental value for ω, we get Re(ϵ'/ϵ) = $(1.11 \pm 0.91) \times 10^{-3}$.

Our calculation is sufficiently far from physical kinematics, that it is not appropriate to compare these results with experiment.[1] Instead, our objective is to show how

well our method performs. We have been able to calculate Re(A_0), the key element needed to explain the $\Delta I = 1/2$ rule, with a 25% statistical error. Comparing our results for Re(A_0) obtained on subsamples of $N = 100$, 400 and all 800 configurations we find that the statistical errors on the quantities we measure do indeed scale as $1/\sqrt{N}$. Therefore, we believe that our nonzero signal for Re(A_0) is real and that we could reduce this statistical error to 10% by quadrupling the size of our sample to 3200 configurations. It is interesting to note the results for primed (disconnected graphs omitted) and unprimed (all graphs included) quantities contributing to Re(A_0) have similar values suggesting that the disconnected graphs, while contributing significantly to the statistical error, have an effect on the final result for Re(A_0) at or below 25%.

In contrast, the result for Im(A_0) has an 80% error. Thus, it is not clear whether the size of the result will survive a quadrupling of the sample with its statistical error reducing to a 40% error or whether the result itself will shrink, remaining statistically consistent with zero. Considering the substantial systematic errors associated with our small volume and the fact that our kinematics are far from the physical, we present this trial calculation as a guideline for future work and a proof of method rather than giving accurate numbers to compare with experiment.

From our observation of the around-the-world effect, we conclude that it is important to use the average of quark propagators obeying periodic and antiperiodic boundary conditions to extend the lattice size in the time direction. In addition, explicit subtraction of the divergent mixing term $\bar{s}\gamma^5 d$ is necessary even for kinematics which are literally energy conserving because the around-the-world path and possibly other excited state matrix elements are far off shell and can be substantially enhanced by such a divergent contribution. Finally, future work should be done using a much larger lattice which can contain two pions without any worry about finite size effects.

The focus of this paper is on developing techniques capable of yielding statistically meaningful results from the challenging lattice correlation functions involved in the amplitude A_0. However, there are other important problems that will also require careful attention if physically meaningful results are to be obtained for this amplitude with an accuracy of better than 20%. Two important issues are associated with operator mixing. As discussed in Appendix A, a proper treatment of the nonperturbative renormalization of the four independent (8, 1) four-quark operators requires that additional operators containing gluonic variables (some of which are not gauge invariant) be included. While including such operators is in principle possible and the subject of active research, controlling such mixing using RI/MOM methods offers significant challenges.

A second problem is operator mixing induced by the residual chiral symmetry breaking of the DWF

---

[1]A further unphysical aspect of our kinematics is the inequality of the strange quark mass used in the fermion determinant and the self contractions appearing in the eye graphs ($m_s = 0.032$) and strange quark masses used in the valence propagator of the K meson ($m_s = 0.066$, 0.99 and 0.165).

formulation. The mixing of such wrong-chirality operators should be suppressed by a factor of order m_{res}. However, the $K \rightarrow \pi\pi$ matrix elements of the important (8, 1) four-quark operators are themselves suppressed by at least one power of m_K^2, a suppression that is absent from similar matrix elements of the induced, wrong-chirality operators. Therefore, such mixing has been ignored in this paper because its effect on the matrix elements of interest are expected to be of order $m_{\text{res}}/m_s \approx 0.08$, suggesting that these effects will be smaller than our 25% statistical errors. To perform a more accurate calculation in the future, these mixing effects may be further suppressed by adopting a gauge action with smaller residual chiral symmetry breaking. For example, this ratio reduces to 0.04 for the DSDR gauge action now being used in RBC/UKQCD simulations [28] and to 0.023 for those ensembles with the smallest lattice spacing created to date using the Iwasaki gauge action [29]. When greater accuracy is required, either an improved fermion action, larger L_s or explicit subtraction of wrong-chirality mixing must be employed.

As we move closer to the physical pion mass we must overcome a further important difficulty: giving physical relative momentum to the two pions. This can be accomplished while keeping the two-pion state in which we are interested as the ground state, if the kaon is given nonzero spatial momentum relative to the lattice. In this case, the lowest energy final state can be arranged to have one pion at rest while the other pion carries the kaon momentum, as in the $\Delta I = 3/2$ calculation of Ref. [30]. However, this requires the momentum carried by the initial kaon and final pion to be 739 MeV, which is 5.4 times larger than the physical pion mass. Such a large spatial momentum will likely make the calculation extremely noisy. For the $\Delta I = 3/2$ calculation, it is possible to use antiperiodic boundary conditions in one or more spatial directions for one of the light quarks so that each pion necessarily carries the physical, 206 MeV momentum present in the actual decay while the kaon can be at rest [12,13]. However, this approach cannot be used in the case of the $I = 0$ final state being studied here. Instead, the use of G-parity boundary conditions [31] may be the solution to this problem.

APPENDIX A: OPERATOR NORMALIZATION

In order to combine our lattice matrix elements with the Wilson coefficients describing the short-distance weak interaction physics responsible for $K \rightarrow \pi\pi$ decay, we must convert our lattice operators into those normalized according to that $\overline{\text{MS}}$ scheme in which the Wilson coefficients are evaluated. We will discuss the details of this procedure in this appendix.

The first step is converting the lattice operators into those normalized according to the RI/MOM scheme [15]. We follow the procedure of Ref. [6] and make use of the fact that the 10 operators which enter the conventional expression given in Eq. (4) are linearly dependent and can be reduced to a set of seven independent operators, Q_1', Q_2', Q_3', Q_5', Q_6', Q_7' and Q_8' defined in Eqs. 172–175 of Ref. [6]. These have been defined so that the resulting operators belong to specific irreducible representations of $SU_L(3) \times SU_R(3)$. The operator Q_1' transforms as a (27, 1). The four operators Q_2', Q_3', Q_5' and Q_6' all belong to the (8, 1) representation, while Q_7' and Q_8' each transform as an (8, 8). Here (m, n) denotes the product of an m-dimensional irreducible representation of $SU_L(3)$ with an n-dimensional irreducible representation of $SU_R(3)$. We refer to the basis of these seven independent operators as the chiral basis. Because $SU_L(3) \times SU_R(3)$ is an exact symmetry of the large momentum, massless limit which our nonperturbative renormalization calculation is intended to approximate, the mixing matrix $Z^{\text{lat}\rightarrow\text{RI}}$ given in Eq. (22), which relates the lattice and RI-normalized operators will be block diagonal, only connecting operators which belong to the same irreducible representation of $SU_L(3) \times SU_R(3)$.

The RI/MOM conditions which define the operators O_i^{RI} and determine the 7×7 matrix $Z^{\text{lat}\rightarrow\text{RI}}$ are imposed on the Green's functions[2]:

$$G_i(p_1, p_2)^f_{\alpha\beta\gamma\delta} = \prod_{i=1}^{4}\Bigg\{\int d^4x_i\Bigg\}\langle s(x_1)_\alpha f(x_2)_\beta Q_i^{\text{RI}}(0)\bar{d}_\gamma(x_3)$$
$$\times \bar{f}_\delta(x_4)\rangle e^{-ip_2(x_1+x_2)}e^{ip_1(x_3+x_4)} \qquad \text{(A1)}$$

evaluated for $p_1^2 = p_2^2 = (p_1 - p_2)^2 = \mu^2$. Here α, β, γ and δ are spin and color indices. The fields $\bar{d}$ and $\bar{f}$ create a down quark and a quark of flavor $f = u$ or d while s and f destroy a strange quark and a quark of flavor f. The RI/MOM conditions are imposed by removing the four

---

[2]While this equation agrees with Eqs. 143 and 152 of Ref. [6], a different choice of momenta was actually used in that earlier reference. These two equations accurately describe the earlier kinematics only after one pair of the momenta p_1 and p_2 are exchanged: $p_1 \leftrightarrow p_2$.

external quark propagators from the amplitudes in Eq. (A1), and then contracting each of the resulting seven amputated Green's functions obtained from Eq. (A1) with seven projectors $\{\Gamma^{ij;f}_{\alpha\beta\gamma\delta}\}_{1\leq j\leq 7}$. The matrix $Z^{\text{lat}\to\text{RI}}$ is then determined by requiring that the resulting 49 quantities take their free field values, as is described in detail in Refs. [6,16].

The choice of external momenta specified by Eq. (A1) is nonexceptional since no partial sum of these momenta vanish (if their signs are chosen so that all four momenta are incoming) and is the choice used in Refs. [16,26]. Such a choice of kinematics is expected to result in normalization conditions which are less sensitive to nonzero quark masses and QCD vacuum chiral symmetry breaking than would be the case if an exceptional set of momenta had been used [32]. The resulting matrix $Z^{\text{lat}\to\text{RI}}(\mu, a)/Z_q^2$ obtained for $\mu = 2.15$ GeV in Ref. [26] is given in Table VII.

Since these RI/MOM renormalization conditions are being imposed for off-shell, gauge-fixed external quark lines, we must in principle include a larger number of operators than the minimal set of seven independent operators which can represent all gauge-invariant matrix elements between physical states of H_W. Therefore, we must also employ a correspondingly larger set of conditions to distinguish among this larger set of operators. These additional operators are two-quark operators of dimension three, four and six and are either gauge-invariant or non gauge-invariant. The treatment of those operators of dimension three and four follows closely that given in Ref. [6]. Equations (12) and (89) of Ref. [16] give a complete list of the corresponding gauge-invariant operators of dimension six. If evaluated between on-shell states, however, these additional operators can be expressed by linear combinations of the seven operators Q_i'.[3] Thus, as stated in Sec. V, the relations given in Eq. (22) between the seven lattice and the seven RI operators are valid only when those operators appear in physical matrix elements between on-shell states. For this equation to be valid when the operators appear in the off-shell, gauge-fixed Green's functions that define the RI scheme, additional RI/MOM-normalized operators must be added.

This is the meaning of the 7×7 matrix $Z^{\text{lat}\to\text{RI}}$ matrix given in Table VII: gauge symmetry and the equations of motion must be imposed to reduce to seven the RI-normalized operators to which the seven lattice operators are equated. In the calculation of $Z^{\text{lat}\to\text{RI}}$ presented in Ref. [26] all such extra, dimension six operators are neglected. For all but one, this might be justified for the current calculation because these operators enter only at

two loops or beyond and the perturbative coefficients that we are using in later steps are computed at only one loop. A single operator, given in Eq. 146 of Ref. [6] and Eq. 12 of Ref. [16] does appear at one loop but has also been neglected because it is expected to give a smaller contribution than other two-quark operators with quadratically divergent coefficients whose effects are indeed small. While these contributions of such extra operators are believed to be small for the current calculation, care must be taken in future calculations in which a continuum limit is attempted that any neglected counter terms with coefficients of the form $\log(\mu a)$ do not become important.

A final imperfection in the results presented in Table VII is that the subtraction of a third dimension-four, two-quark operator which contains a total derivative was not performed. However, the effect of subtracting this third operator is expected to be similar to those of the two operators which were subtracted, effects which were not visible outside of the statistical errors (see *e.g.* Tabs. XIV and XVIII in Ref. [6].)

In the second step, we convert the seven *RI* operators obtained above into the $\overline{\text{MS}}$ scheme:

$$Q_i^{\overline{\text{MS}}} = \sum_j (1 + \Delta r^{\text{RI}\to\overline{\text{MS}}})_{ij} Q_j^{\text{RI}}. \tag{A2}$$

Here, the indices i and j run over the set $\{1, 2, 3, 5, 6, 7, 8\}$ corresponding to the chiral basis of the operators Q_j defined above and a set of operators $Q_j^{\overline{\text{MS}}}$, with identical chiral properties, which are defined in Ref. [16]. We use the computational framework described in Ref. [16] and the resulting 7×7 matrix $\Delta r^{\text{RI}\to\overline{\text{MS}}}$ is given in Table VIII of that reference. As in the case of Eq. (22), the two sets of seven RI and $\overline{\text{MS}}$ operators are related by this 7×7 matrix only when appearing in physical matrix elements. Since the values in this table were obtained for the case that the wave function renormalization constant for the quark field is the quantity $Z_q^{\not\!q}$ it is that factor which we use to extract $Z^{\text{lat}\to\text{RI}}$ from the matrix $Z^{\text{lat}\to\text{RI}}/Z_q^2$ given in Table VII. For our $\beta = 2.13$, Iwasaki gauge ensembles $Z_q^{\not\!q} = 0.8016(3)$. (Note, $Z_q^{\not\!q}$ is the same as the quantity Z_q' introduced in earlier, exceptional momentum schemes [33]).

A third and final step is needed before we can combine the Wilson coefficients with the matrix elements determined in our calculation to obtain the physical amplitudes A_0 and A_2. The 7×7 matrix given in Table VIII of Ref. [16] gives us $\overline{\text{MS}}$ operators defined in the chiral basis. However, the Wilson coefficients which are available in Ref. [17] are defined for the ten-operator basis referred to as basis I in Ref. [16]. The conversion between the linearly independent, seven operator basis and the conventional set of ten linearly dependent operators is correctly given by the application of simple Fierz identities for the case of the lattice and RI/MOM operators. As is explained, for example, in Ref. [16], this procedure is more complex for

---

[3]Exceptions to this statement come from the two dimension-three, mass operators $\bar{s}(1 \pm \gamma^5)d$ which do contribute independently to on-shell matrix elements in which four-momentum is not conserved.

TABLE VII.   The renormalization matrix $Z^{\text{lat}\to\text{RI}}/Z_q^2$ in the seven operator chiral basis at the energy scale $\mu = 2.15$ GeV. These values were obtained from Ref. [26] by performing an error weighted average of the values given in Tabs. 40, 41 and 42 (corresponding to bare quark masses of 0.01, 0.02 and 0.03) and inverting the resulting matrix with an uncorrelated propagation of the errors. Since the results given in these three tables are equal within errors, we chose to combine them to reduce their statistical errors rather than to perform a chiral extrapolation.

	1	2	3	4	5	6	7
1	0.825(7)	0.	0.	0.	0.	0.	0.
2	0.	0.882(38)	−0.111(41)	−0.009(12)	0.010(10)	0.	0.
3	0.	−0.029(69)	0.962(92)	0.013(22)	−0.011(25)	0.	0.
4	0.	−0.04(12)	−0.01(13)	0.924(42)	−0.149(35)	0.	0.
5	0.	0.17(18)	0.08(23)	−0.042(55)	0.649(63)	0.	0.
6	0.	0.	0.	0.	0.	0.943(8)	−0.154(9)
7	0.	0.	0.	0.	0.	−0.0636(53)	0.680(11)

operators defined using $\overline{\text{MS}}$ normalization. Here subtleties of defining γ^5 in dimensions different from four, result in ten $\overline{\text{MS}}$-normalized operators, $Q_i^{\overline{\text{MS}}}$, which are not related by the usual Fierz identities, with Fierz violating terms appearing at order α_s.

Thus, the conventional ten $\overline{\text{MS}}$-normalized operators $Q_i^{\overline{\text{MS}}}$ which appear in Eq. (4) must be constructed, again through one-loop perturbation theory, from the seven operators $Q_i'^{\overline{\text{MS}}}$:

$$Q_i^{\overline{\text{MS}}} = \sum_j (T + \Delta T_I^{\overline{\text{MS}}})_{ij} Q_j'^{\overline{\text{MS}}}, \qquad (A3)$$

in the notation of Ref. [16]. The 10×7 matrices, T and $\Delta T_I^{\overline{\text{MS}}}$ are given in Eqs. 59 and 65 of that reference. (The subscript I on the matrix $\Delta T_I^{\overline{\text{MS}}}$ identifies the particular ten-operator, $\overline{\text{MS}}$ basis required by the Wilson coefficients of Ref. [17].)

This entire set of nonperturbative and perturbative transformations can be summarized by the following equation which expresses the 10 $\overline{\text{MS}}$-normalized operators $Q_i^{\overline{\text{MS}}}$ in terms of the seven, chiral basis, lattice operators whose matrix elements we actually compute:

TABLE VIII.   Wilson Coefficients in the $\overline{\text{MS}}$ scheme, at energy scale $\mu = 2.15$ GeV.

i	$y_i^{\overline{\text{MS}}}(\mu)$	$z_i^{\overline{\text{MS}}}(\mu)$
1	0	−0.298 29
2	0	1.144 39
3	0.024 141	−0.002 438 27
4	−0.058 121	0.009 951 57
5	0.010 2484	−0.001 105 44
6	−0.069 971	0.006 574 57
7	−0.000 211 182	0.000 070 1587
8	0.000 779 244	−0.000 089 9541
9	−0.010 6787	0.000 015 0176
10	0.002 9815	0.000 065 6482

$$Q_i^{\overline{\text{MS}}} = \sum_j [(T + \Delta T_I^{\overline{\text{MS}}})_{10\times 7}(1 + \Delta r^{\text{RI}\to\overline{\text{MS}}})_{7\times 7}$$
$$\times (Z^{\text{lat}\to\text{RI}})_{7\times 7}]_{ij} Q_j^{\text{lat}} \qquad (A4)$$

$$= \sum_j [(Z^{\text{lat}\to\overline{\text{MS}}})_{10\times 7}]_{ij} Q_j^{\text{lat}}, \qquad (A5)$$

where the subscripts indicate the dimensions of the matrices being multiplied and the matrix $Z_{ij}^{\text{lat}\to\overline{\text{MS}}}$ is used in Eq. (25).

The physical matrix elements listed in Tables II and V are obtained by using Eq. (A5) to determine the matrix elements of the 10 conventional operators $Q_i^{\overline{\text{MS}}}$ in term of the matrix elements of the seven lattice operators Q_j. These 10 matrix elements are then combined with the 20 Wilson coefficients computed for the renormalization scale $\mu = 2.15$ GeV using the formulae in Ref. [17]. The values obtained for these Wilson coefficients are listed in Table VIII.

Note, there are many important details of the RI/MOM renormalization procedure, such as the subtraction of dimension three and four operators, which are not repeated here because they are already discussed with some care in Refs. [6,16].

APPENDIX B: PROPAGATOR SOURCES

The calculations presented in this paper rely on propagators computed using two types of sources. The propagators for the quarks which make up the initial and final state mesons are constructed from Coulomb gauge-fixed wall sources, while the fermion loops appearing in the eye diagrams are formed from propagators using random Gaussian wall sources. In this appendix, we specify how each of these sources is constructed. (Our conventions for the five-dimensional Dirac operator D and its coupling to the gauge field are given in Ref. [34]t.)

A Coulomb gauge-fixed wall source located at the time t_w with spin α and color a is a five-dimension color and spin vector field $\mathcal{C}(\vec{x}, t, s; t_w, \alpha, a)_{\beta, b}$ with spinor and color indices β and b and is given by:

$$
\mathcal{C}(\vec{x}, t, s; t_w, \alpha, a)_{\beta, b} = \left\{ \left(\frac{1 + \gamma^5}{2} \right)_{\beta, \alpha} \delta_{s, L_s - 1} \right.
$$
$$
\left. + \left(\frac{1 - \gamma^5}{2} \right)_{\beta, \alpha} \delta_{s, 0} \right\} \delta_{t, t_w} V^C(\vec{x}, t)_{b, a}^\dagger
$$
(B1)

where $V^C(\vec{x}, t)$ is the 3×3 local gauge transformation matrix that transforms the gauge links $U_i(\vec{x}, t)$ into links $U_i^C(\vec{x}, t)$ in Coulomb gauge:

$$
U_i^C(\vec{x}, t) = V^C(\vec{x}, t) U_i(\vec{x}, t) V^C(\vec{x} + \hat{e}_i a, t)^\dagger.
$$
(B2)

Here, $\hat{e}_i$ is a unit vector in the ith direction.

The color and spinor field $\mathcal{C}(\vec{x}, t, s; t_w, \alpha, a)_{\beta, b}$ is used to define a five-dimensional propagator $G(\vec{x}, t, s; t_w, \alpha, a)_{b, \beta}$ which obeys the domain wall fermion Dirac equation:

$$
\sum_{x', t', s'} \{ D_{\vec{x}, t, s; \vec{x}', t', s'} G(\vec{x}', {}^\prime t, s'; t_w, \alpha, a) \}_{\beta, b}
$$
$$
= \mathcal{C}(\vec{x}, t, s; t_w, \alpha, a)_{\beta, b},
$$
(B3)

using the notation of Ref. [34]. Following those conventions, we can project the five-dimensional propagator G onto the four-dimensional walls to construct the four-dimensional propagators L and S for the light and strange quarks used in Eqs. (1) and (9)–(11). For example, the light quark propagator is constructed as follows:

$$
L(\vec{x}, t; t_w)_{\beta, b; \alpha, a} = \left\{ \frac{1 + \gamma^5}{2} G(\vec{x}, t, L_s - 1; t_w, \alpha, a) \right\}_{\beta, b}
$$
$$
+ \left\{ \frac{1 - \gamma^5}{2} G(\vec{x}, t, 0; t_w, \alpha, a) \right\}_{\beta, b}.
$$
(B4)

Critical to this approach is the limited gauge covariance of Eq. (B3) under general gauge transformations of the underlying gauge configuration. This gauge covariance can be seen by considering a gauge transformation

$$
U_\mu(x) \rightarrow U_\mu^V(x) = V(x) U_\mu(x) V(x + \hat{e}_\mu a)^\dagger
$$
(B5)

where $x = (\vec{x}, t)$ identifies a four vector and links in the general space-time direction μ are being transformed. The gauge covariance of Eq. (B3) can be established if we view the Coulomb gauge transformation matrices $V^C[\{U\}](x)$ which appear in the source $\mathcal{C}$ as functionals of the gauge ensemble from which they were defined and observe that candidate Coulomb gauge transformation matrices for the

transformed links can be easily constructed from the original Coulomb gauge transformation matrices $V^C[\{U\}]$ as

$$
V^C[\{U^V\}](x) = \mathcal{G} V^C[\{U\}](x) V(x)^\dagger
$$
(B6)

where $\mathcal{G}$ is a 3×3 position-independent, global gauge transformation. If the original matrices $V^C[\{U\}](x)$ transform the configuration $\{U\}$ to Coulomb gauge, then by construction, the new matrices $V^C[\{U^V\}](x)$ will do the same for the gauge-transformed links $\{U^V\}$. Thus, if Eq. (B6) holds, the left- and right-hand sides of Eq. (B3) transform similarly under the gauge transformation of Eq. (B5) (recall that $G(x, s; t_w)$ will also transform as a color vector at x).

However, there are two issues that must be addressed. First the global gauge transformation $\mathcal{G}$ transforms the right-hand indices of the $(V^C)^\dagger$ on the right-hand side of Eq. (B3) but does not appear on the left-hand side when a gauge transformation is performed. Nevertheless, this lack of invariance under a general gauge transformation can be removed if the propagators $G(\vec{x}, t, s; t_w, \alpha, a)_{\beta, b}$ always appear in products in which the source color indices a are arranged in gauge-invariant combinations. Second, the Coulomb gauge transformation for the gauge-transformed configuration can be guaranteed to be given by Eq. (B6) only if the transformation to Coulomb gauge is unique up to a global gauge transformation, an assumption violated by Gribov copies. Thus, we expect hadronic propagators constructed from these Coulomb gauge-fixed wall sources to be affected by gauge noise generated by Gribov copies. However, in practice we find these are excellent sources for creating pseudoscalar mesons providing good statistics from volume averaging and long plateaus when the effective mass of the mesons is examined.

The construction of the random Gaussian wall sources is more straightforward. As described earlier, a separate random source is generated for each spin-color pair α, a. Thus, a random Gaussian wall source at the time t_w with spin α and color a is given by the five-dimensional spin-color vector

$$
\mathcal{R}(\vec{x}, t, s; t_w, \alpha, a)_{b, \beta} = \eta(\vec{x}, t) \delta_{t, t_w} \delta_{a, b} \left[\left(\frac{1 + \gamma^5}{2} \right)_{\alpha, \beta} \delta_{s, L_s - 1} \right.
$$
$$
\left. + \left(\frac{1 - \gamma^5}{2} \right)_{\alpha, \beta} \delta_{s, 0} \right]
$$
(B7)

where $\eta(\vec{x}, t)$ are independent Gaussian random numbers defined for each space-time point. An independent set of random numbers, $\eta(\vec{x}, t)$ is generated each of the 12 separate sources corresponding to the 12 possible choices of spin (α) and color (a). The corresponding propagators G^R and L^R are constructed in a fashion completely analogous to that described above for G, L and S in Eqs. (B3) and (B4).

[1] M. Gaillard and B. W. Lee, Phys. Rev. Lett. **33**, 108 (1974).

[2] G. Altarelli and L. Maiani, Phys. Lett. B **52**, 351 (1974).

[3] K. Nakamura *et al.* (Particle Data Group), J. Phys. G **37**, 075021 (2010).

[4] S. Li and N. H. Christ, Proc. Sci., LATTICE2008 (2008) 272.

[5] J. Laiho and R. S. Van de Water, Proc. Sci., LATTICE2010 (2010) 312.

[6] T. Blum *et al.* (RBC), Phys. Rev. D **68**, 114506 (2003).

[7] J. I. Noaki *et al.* (CP-PACS), Phys. Rev. D **68**, 014501 (2003).

[8] M. Golterman and E. Pallante, J. High Energy Phys. 10 (2001) 037.

[9] M. Golterman and E. Pallante, Phys. Rev. D **69**, 074503 (2004).

[10] C. Aubin *et al.*, Phys. Rev. D **74**, 034510 (2006).

[11] N. H. Christ *et al.*, Phys. Rev. Lett. **105**, 241601 (2010).

[12] E. J. Goode and M. Lightman, Proc. Sci., LATTICE2010 (2010) 313.

[13] C. Kim, Nucl. Phys. B, Proc. Suppl. **129**, 197 (2004).

[14] C. T. Sachrajda and G. Villadoro, Phys. Lett. B **609**, 73 (2005).

[15] G. Martinelli, C. Pittori, C. T. Sachrajda, M. Testa, and A. Vladikas, Nucl. Phys. **B445**, 81 (1995).

[16] C. Lehner and C. Sturm, Phys. Rev. D **84**, 014001 (2011).

[17] G. Buchalla, A. J. Buras, and M. E. Lautenbacher, Rev. Mod. Phys. **68**, 1125 (1996).

[18] L. Lellouch and M. Luscher, Commun. Math. Phys. **219**, 31 (2001).

[19] C. W. Bernard and A. Soni, Nucl. Phys. B, Proc. Suppl. **9**, 155 (1989).

[20] C. Dawson *et al.*, Nucl. Phys. **B514**, 313 (1998).

[21] C. Allton *et al.* (RBC and UKQCD), Phys. Rev. D **76**, 014504 (2007).

[22] C. Allton *et al.* (RBC-UKQCD), Phys. Rev. D **78**, 114509 (2008).

[23] L. Giusti, C. Hoelbling, M. Luscher, and H. Wittig, Comput. Phys. Commun. **153**, 31 (2003).

[24] M. Lightman (RBC), Proc. Sci., LATTICE2008 (2008) 273.

[25] Q. Liu (RBC), Proc. Sci., LAT2009 (2009) 101.

[26] S. Li, Ph.D. thesis, Columbia University, 2008, aAT-3333388.

[27] M. Luscher, Nucl. Phys. **B354**, 531 (1991).

[28] D. Renfrew, T. Blum, N. Christ, R. Mawhinney, and P. Vranas, Proc. Sci., LATICE2008 (2008) 048.

[29] Y. Aoki *et al.* (RBC Collaboration, UKQCD Collaboration), Phys. Rev. D **83**, 074508 (2011).

[30] T. Yamazaki (RBC), Phys. Rev. D **79**, 094506 (2009).

[31] C.-h. Kim and N. H. Christ, Nucl. Phys. B, Proc. Suppl. **119**, 365 (2003).

[32] Y. Aoki *et al.*, Phys. Rev. D **78**, 054510 (2008).

[33] C. Sturm *et al.*, Phys. Rev. D **80**, 014501 (2009).

[34] T. Blum, P. Chen, N. H. Christ, C. Cristian, C. Dawson *et al.*, Phys. Rev. D **69**, 074502 (2004).